

1 **Presynaptic APP levels and synaptic homeostasis are regulated by Akt phosphorylation of**
2 **Huntingtin**

3

4 Julie Bruyère^{1,3}, Yah-Se Abada^{2,3}, H  l  ne Vitet^{1,3}, Ga  lle Fontaine², Jean-Christophe Deloulme¹, Aur  lia
5 C  s², Eric Denarier¹, Karin Pernet-Gallay¹, Annie Andrieux¹, Sandrine Humbert¹, Marie Claude Potier²,
6 Beno  t Delatour², Fr  d  ric Saudou^{1,4,*}

7

8 ¹Univ. Grenoble Alpes, Inserm, U1216, CHU Grenoble Alpes, CEA, Grenoble Institut Neurosciences,
9 38000 Grenoble, France.

10 ²Institut du Cerveau et de la Moelle   pini  re, ICM, Inserm U1127, CNRS UMR 7225, Sorbonne
11 Universit  , F-75013, Paris, France

12 ³These authors contributed equally

13 ⁴Lead contact

14 *Correspondence: frederic.saudou@inserm.fr

15

16 **running title:** APP-mediated synapse homeostasis requires HTT

17

18 **Abstract**

19 Studies have suggested that amyloid precursor protein (APP) regulates synaptic homeostasis, but the
20 evidence has not been consistent. In particular, signaling pathways controlling APP transport to the
21 synapse in axons and dendrites remain to be identified. Having previously shown that Huntingtin (HTT),
22 the scaffolding protein involved in Huntington's disease, regulates neuritic transport of APP, we used a
23 microfluidic corticocortical neuronal network-on-a-chip to examine APP transport and localization to the
24 pre- and post-synaptic compartments. We found that HTT, upon phosphorylation by the Ser/Thr kinase
25 Akt, regulates APP transport in axons but not dendrites. Expression of an unphosphorylatable HTT
26 decreased axonal anterograde transport of APP, reduced presynaptic APP levels, and increased synaptic
27 density. Ablating *in vivo* HTT phosphorylation in APPPS1 mice, which overexpress APP, reduced
28 presynaptic APP levels, restored synapse number and improved learning and memory. The Akt-HTT
29 pathway and axonal transport of APP thus regulate APP presynaptic levels and synapse homeostasis.

30

31

32 **Key words:**

33 Amyloid precursor protein, Huntingtin, axonal transport, dendritic transport, synapse, microfluidics, Akt
34 phosphorylation, cortex, hippocampus, APPPS1 mice

35

36

37 **Introduction**

38 Synaptic homeostasis stabilizes neural circuits and ensures faithful communication within networks that
39 are being continuously remodeled. It involves a complex interplay between presynaptic and postsynaptic
40 proteins that modulates synaptic morphology and strength (Sudhof, 2018). Several studies suggest that
41 amyloid precursor protein (APP) contributes to synapse homeostasis (for reviews see (Hoe et al., 2012;
42 Muller et al., 2017), and although the evidence is not entirely consistent, this possibility has intuitive
43 appeal because of APP's involvement in diseases of cognition (e.g., Alzheimer's disease, Lewy body
44 dementia, and cerebral amyloid angiopathy)(Muller et al., 2017). Some studies suggest that loss of APP
45 reduces synapse density (Weyer et al., 2014), while others show that it increases the number of synapses
46 (Bittner et al., 2009). More firmly established is the fact that APP is transported both in axons and
47 dendrites and localizes in both the pre- and post-synaptic compartments, where it could associate with
48 synaptic release machinery to regulate neuronal transmission (Buggia-Prevot et al., 2014; Das et al., 2016;
49 Fanutza et al., 2015; Groemer et al., 2011; Klevanski et al., 2015). In addition, APP may function as an
50 adhesion molecule at the synapse (Muller et al., 2017; Soba et al., 2005). Any modification in the
51 transport of APP in either axons or dendrites thus has the potential to disrupt synaptic function or
52 homeostasis. Therefore, there is a need to identify mechanisms and/or pathways that specifically regulate
53 APP transport both in axons and/or dendrites and to determine whether manipulating these pathways
54 control APP accumulation and synapse homeostasis.

55 APP is transported from the Golgi apparatus to the synapse in either dendrites or axons, and in both
56 anterograde and retrograde directions by kinesin-1 and dynein, respectively (Brunholz et al., 2011; Gibbs
57 et al., 2015; Toh and Gleeson, 2016). We and others have shown that wild-type huntingtin (HTT), but not
58 the polyglutamine-expanded HTT that causes Huntington's disease (HD), facilitates APP transport by
59 increasing the velocity of APP-containing vesicles (Colin et al., 2008; Her and Goldstein, 2008). HTT is
60 a large scaffold protein that interacts with various protein complexes including molecular motor proteins
61 and, regulates consequently the transport of several cargos (Saudou and Humbert, 2016). APP transport
62 into neurites is altered upon reduction of HTT levels or by the presence of polyQ expansion on HTT
63 (Colin et al., 2008; Her and Goldstein, 2008). However, these studies did not distinguished axons from
64 dendrites and did not investigate the consequences on APP levels at the synapse both in vitro and in vivo.
65 Consequently, several questions remain to be addressed regarding the interplay between HTT and APP
66 and its physiological consequences.

67 To answer these questions, we studied APP and HTT in a microfluidic device that reconstitutes a
68 corticocortical neuronal network with separate presynaptic, synaptic, and postsynaptic compartments, and
69 further tested our findings in APPPS1 mice, which display AD-like pathology. We find that subtle

70 modifications of axonal transport of APP change synaptic levels of APP and have dramatic consequences
71 on synapse function.

72

73 **Results**

74 **Developing an *in vitro* corticocortical network using microfluidic chambers**

75 One of the major impediments to assessing APP transport in axons and dendrites under physiological
76 conditions is the difficulty of recreating a mature neuronal network in a dish. Primary cultures are usually
77 randomly distributed, with multidirectional, random connections. The use of Campenot chambers or
78 microfluidic devices made it possible to separate axons from dendrites and soma, but neurons in these
79 chambers are still not integrated into networks as they would be *in vivo* (Taylor et al., 2005). We therefore
80 turned to later-generation devices (Taylor et al., 2010) and modified them to reconstitute an oriented
81 network with optimized connections (Moutaux et al., 2018; Virlogeux et al., 2018). These devices contain
82 three compartments (presynaptic, synaptic, and postsynaptic) that are fluidically isolated and separated by
83 microchannels that are 5- μm high and 5- μm wide, but of two different lengths: 500 μm and 75 μm
84 (**Figure 1A**). The 500 μm channels allow only axons from the presynaptic compartment to reach the
85 synaptic compartment (Taylor et al., 2005). The 75 μm long microchannels allow dendrites to cross from
86 the postsynaptic to the synaptic compartment, where MAP2 staining shows they connect with axons
87 coming from the presynaptic compartment (**Figure 1B**). We reconstructed a corticocortical network-on-a-
88 chip since APP protein is expressed in the cortex, and AD largely targets iso- and archicortical brain
89 regions. In these microfluidic devices, we observed full maturation of the corticocortical neuronal
90 network between days *in vitro* (DIV) 10 and 15, as revealed by uptake of FM4-64, an indicator of
91 endocytosis/exocytosis of functional synapses (**Figure 1C**). This device is thus optimized for studying the
92 sub-cellular dynamics of APP.

93

94 **APP is transported to synapses from both pre- and post-synaptic neurons**

95 We transduced mouse cortical neurons at DIV 8 with lentiviruses expressing APP tagged with
96 mCherry at the C terminus (APP-mCherry), which retains APP characteristics (Kaether et al., 2000;
97 Marquer et al., 2014). We recorded the movements of APP-mCherry vesicles at high frequency frame rate
98 using spinning disk confocal microscopy and found that velocities reach a maximum at DIV13, when the
99 network is fully mature, with established synapses (**Figure 1B and C, Figure 1-figure supplement 1**).
100 To assess axonal transport, we first focused on the distal part of the 500- μm long microchannels (**Figure**
101 **1B**) to follow APP-mCherry transduced in the presynaptic compartment (**Figure 2A, Video 1**), which can
102 be reached only by presynaptic axons (Moutaux et al., 2018; Taylor et al., 2005; Virlogeux et al., 2018).
103 To assess dendritic transport of mCherry vesicles, we transfected the postsynaptic neurons with a MAP2-

104 GFP plasmid and selected only the mCherry vesicles that crossed the 75- μ m-long microchannels (**Figure**
105 **2A, Video 2**). MAP2-GFP transfection did not modify the transport of APP by itself (data not shown).

106 We generated kymographs from the axonal and dendritic recordings (**Figure 2B**) and measured
107 several transport parameters (see Materials and Methods): the velocity of APP vesicles, their number, and
108 the cumulative distance they travelled in anterograde and retrograde directions within axons. We defined
109 the overall direction of APP vesicle transport in axons by adding the anterograde cumulative distance to
110 the negative retrograde cumulative distance, so that positive values indicate a net anterograde flux from
111 the soma towards the synapse (**Figure 2B**). We also measured dendritic transport, expressed as inward
112 (from postsynaptic compartment to soma) or outward (from soma to postsynaptic site), since
113 microtubules in dendrites (unlike in axons) are not fully oriented with the plus ends towards the dendrite's
114 extremities (Kapitein and Hoogenraad, 2015; van Beuningen and Hoogenraad, 2016)(**Figure 2B**). Our
115 analysis showed a net anterograde axonal and outward dendritic flux for APP-containing vesicles,
116 indicating that there is a significant transport of APP to the synapse from both pre- and postsynaptic
117 neurons (**Figure 2B**). These findings in a mature network are in accordance with the reported velocities
118 of APP vesicles (Fu and Holzbaaur, 2013; Her and Goldstein, 2008; Marquer et al., 2014; Rodrigues et al.,
119 2012; Vagnoni et al., 2013).

120

121 **Huntingtin phosphorylation regulates axonal but not dendritic transport of APP**

122 We had previously shown that phosphorylation of HTT at Serine 421 determines the direction in
123 which various cargoes are transported in neurites (Colin et al., 2008). These experiments over-expressed
124 short HTT fragments containing mutations at Serine 421 in neurons that were randomly cultured (i.e., not
125 integrated into a mature network) and in which axons and dendrites could not be discriminated. To study
126 the role of HTT phosphorylation at S421 in APP transport in axons *versus* dendrites, we took advantage
127 of our microfluidic system and two lines of homozygous knock-in mice: one in which Serine 421 is
128 replaced by an alanine ($Htt^{S421A/S421A}$ or HTT_{SA}), mimicking the absence of phosphorylation, and another
129 in which Serine 421 is replaced by aspartic acid ($Htt^{S421D/S421D}$ or HTT_{SD}), mimicking constitutive
130 phosphorylation (Thion et al., 2015). It is important to note that neither mutation affects the level of HTT
131 expression (Ehinger et al., 2020).

132 We isolated HTT_{SA} and HTT_{SD} cortical neurons from the mice and plated them in both pre- and
133 postsynaptic compartments of our microfluidic device as in **Figure 1A**. Abolishing HTT phosphorylation
134 at Serine 421 increased the velocity of retrograde vesicles, increased their cumulative distance travelled,
135 and reduced the net anterograde flux of APP vesicles in axons (**Figure 3A, Video 3**), whereas HTT_{SD}
136 neurons showed an increase in *anterograde* velocity and greater cumulative distance travelled by APP
137 compared to HTT_{SA} or WT neurons. Nevertheless, the net flux, which reflects the flow of vesicles from

138 the soma to axon terminals, was not significantly different from that observed in WT neurons. This
139 indicates that in our experimental conditions, most of the WT HTT is in its phosphorylated form.
140 Phosphorylation status did not, however, modify WT APP transport in dendrites (**Figure 3B**). We
141 conclude that HTT phosphorylation regulates axonal but not dendritic transport of APP to the synapse.

142 Given that microtubule polarity influences selective cargo trafficking in axons and dendrites (van
143 Beuningen and Hoogenraad, 2016), it is interesting to note that the axon-specific effect of HTT
144 phosphorylation correlates with axons' preferential plus-end microtubule orientation (dendrites have
145 mixed microtubule polarity). To further understand the selective effect in axons versus dendrites, we
146 investigated the interaction of non-phospho HTT with kinesin-1, the molecular motor responsible for the
147 transport of APP (Matsuda et al., 2001; Verhey et al., 2001). Because most WT HTT is already in its
148 phosphorylated form in our experimental conditions, we compared HTT_{SA} with WT (rather than HTT_{SD})
149 neurons. We found no difference between WT and HTT_{SA} neurons in their total kinesin heavy chain
150 (KHC) levels (**Figure 3-figure supplement 1A**), but HTT_{SA} neurons had less KHC in the vesicular
151 fraction than in the cytosolic fraction (**Figure 3-figure supplement 1B**). These results are in agreement
152 with our previous study suggesting HTT dephosphorylation decreases the association of kinesin-1 with
153 vesicles (Colin et al., 2008).

154

155 **HTT regulation of APP anterograde axonal transport is mediated by Akt phosphorylation**

156 HTT phosphorylation at S421 depends on the Akt kinase (Humbert et al., 2002). We therefore
157 investigated whether Akt could modify anterograde transport of APP and whether this required HTT
158 phosphorylation. We transduced cortical neurons with APP-mCherry and a construct encoding
159 constitutively active Akt (Akt-CA) or a form of Akt (Akt-N) that has no kinase activity with and IRES-
160 GFP or the corresponding empty GFP vector (GFP) as a control. As expected, Akt induced endogenous
161 HTT phosphorylation in WT neurons but was unable to do so in HTT_{SA} neurons (**Figure 4A**). In addition,
162 HTT phosphorylation was reduced upon Akt-N expression.

163 To ensure Akt was not affecting neuronal growth and maturation, we transduced neurons at DIV8 and
164 analyzed APP trafficking at DIV13. Expressing Akt-CA and APP-mCherry in wild-type (WT) cortical
165 neurons had no effect on vesicle number but markedly increased anterograde velocity of APP and the
166 cumulative distances travelled by anterograde APP-containing vesicles, which in turn led to an increase of
167 their net anterograde flux (**Figure 4B and 4C, Video 4**). In contrast, in HTT_{SA} neurons, Akt-CA was
168 unable to modify the different transport parameters. Thus, Akt activation increases APP anterograde
169 transport in axons by phosphorylating HTT at Serine 421. These results identify Akt-HTT signaling as a
170 new mechanism that regulates axonal trafficking of APP.

171

172 **Huntingtin-mediated axonal transport determines presynaptic APP levels**

173 To determine whether reduced anterograde axonal transport of APP affects the targeting of APP at the
174 plasma membrane, we used TIRF (total internal reflection fluorescence) microscopy and a super-ecliptic
175 version of pHluorin (SEP) fused to the N-terminal part of APP to monitor insertion of APP into the
176 plasma membrane. As we could not reliably detect APP-SEP at the membrane in primary cultures of
177 neurons, we transfected the APP-SEP construct with versions of full-length wild type HTT (pARIS HTT)
178 (Pardo et al., 2010) or full-length HTT containing the S421A mutation (pARIS HTT_{SA}) into COS cells
179 that are known to have their plus-end microtubules oriented toward the plasma membrane (Takemura et
180 al., 1995). We detected far fewer APP-SEP dots per minute in cells expressing pARIS HTT_{SA} than in cells
181 expressing pARIS HTT (**Figure 5A, Video 5**). This result suggests that reducing transport of APP to the
182 plasma membrane by dephosphorylating HTT decreases APP targeting at the plasma membrane.

183 The fluidic isolation of the synaptic compartment enabled us to collect proteins and investigate
184 the targeting of APP at synapses by measuring APP levels by Western blot. We first verified that the
185 synaptic chamber is enriched with synaptic marker synaptophysin and empty of nuclear marker lamin B1
186 (**Figure 5B**). Lack of HTT phosphorylation led to a reduction of APP protein levels at synapses but no
187 real change in the soma-containing chamber (**Figure 5B**).

188 We then investigated APP targeting *in vivo*. We first prepared synaptosomal fractions from WT
189 mouse brains and purified post-synaptic density fractions (PSD, enriched in postsynaptic proteins) and
190 non-PSD fractions that are enriched with presynaptic proteins. As expected, we detected synaptophysin, a
191 presynaptic marker, and PSD95, a postsynaptic marker, in the non-PSD and PSD enriched fractions,
192 respectively (**Figure 5C**). We detected APP in both fractions. We found that most of the synaptosomal
193 APP was enriched in the non-PSD fraction, which suggests that a significant fraction of APP found at
194 synapses originates from the presynaptic compartment. Since anterograde axonal transport of APP is
195 controlled by HTT phosphorylation, we measured APP within fractions prepared from HTT_{SA}
196 homozygous mouse brains (**Figure 5D**). APP levels were lower in the non-PSD fraction of HTT_{SA} mouse
197 brains (enriched with presynaptic proteins), but APP levels did not differ significantly between WT and
198 HTT_{SA} mouse brains in the PSD fraction (**Figure 5D**). Together, our results indicate that the absence of
199 HTT phosphorylation reduces anterograde transport of APP in axons, but not in dendrites, and
200 subsequently regulates the levels of APP in the presynaptic compartment both *in vitro* and *in vivo*.

201

202 **HTT chronic dephosphorylation alters brain morphology and synapse size and number**

203 The previously generated HTT_{SA} mice have no obvious phenotype but were not fully characterized
204 for brain-related behavior and morphology (Thion et al., 2015). Subsequent analyses of the mice at 6
205 months of age did not reveal any behavioral abnormalities (Ehinger et al., 2020). Given our observation

206 that anterograde transport and presynaptic accumulation of APP are both reduced in HTT_{SA} mice and that
207 APP is associated with late-onset defects, we subjected the mice to complete behavioral analysis
208 (SHIRPA (Rogers et al., 1997), open field, grip test and elevated plus Maze) when they were 12 months
209 old, and again found no significant differences in behavior (**Figure 6-figure supplement 1 and table**
210 **supplement 1**).

211 We then performed anatomical *ex vivo* MRI of young adult WT and HTT_{SA} mice (**Figure 6A and B**).
212 HTT_{SA} mice between 8 and 11 weeks of age showed greater whole brain volume (4.8 %) affecting the
213 hippocampus (8.5%) and the cortex (3.7%) but not the striatum. To determine whether HTT_{SA} produced
214 more subtle changes in synapse number and morphology, we quantified synaptic density and spine size in
215 WT and HTT_{SA} mice by electron microscopy. HTT_{SA} mice had more synapses than WT mice but no
216 difference in spine size (**Figure 6C**).

217 To further investigate the contribution of transport and APP levels on synapse number, we took
218 advantage of the microfluidic devices and, using pre- and post-synaptic markers (synaptophysin and
219 PSD95, respectively), measured the number of synaptic contacts in the synaptic compartment within wild
220 type and HTT_{SA} mature neuronal circuits at DIV12. In agreement with our *in vivo* experiments (**Figure**
221 **6C**), we found an increase in the number of synaptic contacts in the HTT_{SA} circuit (**Figure 7A**).

222 To determine whether APP overexpression would increase the quantity of APP within the presynaptic
223 cortical compartment of a WT or HTT_{SA} network (**Figure 7B**), we transduced WT or HTT_{SA} neurons with
224 a lentivirus expressing APP at DIV7 and measured synapse number at DIV12. Overexpressing APP in
225 WT presynaptic cortical neurons decreased synaptic contacts, but overexpressing APP in HTT_{SA}
226 presynaptic cortical neurons restored synaptic contacts back to the levels seen in WT neurons (**Figure 7B**).
227 The presynaptic level of APP thus appears to determine synapse number and can be modulated by HTT
228 phosphorylation; this further supports a role for the Akt-HTT-APP pathway in synapse homeostasis.

229 To ensure that the HTT_{SA} mutation was not affecting neurodevelopment, we transduced a WT circuit
230 at DIV8, when axon growth has ended (Moutaux et al., 2018), with lentiviruses expressing APP and
231 either an N-terminal HTT construct containing the first 480 amino acids (HTT-480-WT) or a construct in
232 which the S421 has been mutated into alanine (HTT-480-SA). We found that expressing the HTT-480-SA
233 construct in mature neurons led to an increase in synaptic contacts similar to what is observed in HTT_{SA}
234 neurons differentiated in microchambers (**Figure 7A and 7C**). This suggests that the HTT S421A
235 mutation has no major role in axon growth and/or that the increase of synaptic contacts seen in HTT_{SA}
236 neurons is not due to changes in neurodevelopment but rather results from reduced transport and
237 accumulation of APP at the presynapses. We then investigated the effect of APP overexpression in WT
238 neurons. As in **Figure 7B**, APP overexpression in WT neurons transduced with HTT-480-WT led to a
239 decrease in the number of synaptic contacts. However, it had no effect in neurons expressing HTT-480-

240 SA, indicating that HTT dephosphorylation attenuates the effect of APP overexpression on synapse
241 number (**Figure 7D**). We conclude that reducing anterograde axonal transport of APP either during
242 axonal growth or in mature networks is sufficient to modulate synaptic contacts.

243

244 **Unphosphorylatable HTT reduces APP presynaptic levels in APPPS1 mouse model**

245 HTT-mediated transport clearly modulates presynaptic levels of APP in a corticocortical circuit, but
246 we wanted to investigate the consequences of chronic HTT dephosphorylation *in vivo*, in a mouse that
247 overexpresses APP. We chose APPPS1 mice—double transgenics that bear a human APP transgene with
248 the Swedish mutation (APP^{Swe}) and a mutant human presenilin 1 (PS1^{L166P}) transgene (Radde et al.,
249 2006)—which express human APP at three times the level of murine APP and mimic familial
250 Alzheimer's. These mice show reduced synapse density (Alonso-Nanclares et al., 2013; Bittner et al.,
251 2012; Hoe et al., 2012; Muller et al., 2017; Priller et al., 2009; Radde et al., 2006; Zou et al., 2015). We
252 crossed HTT_{SA} phospho-mutant mice with APPPS1 mice to generate APP^{Swe};PS1^{L166P};Htt^{S421A/S421A}
253 mice, heretofore referred to as APPPS1/HTT_{SA} mice.

254 The levels of APP in the non-post-synaptic density fraction of APPPS1/HTT_{SA} mice were
255 significantly lower than in APPPS1 mice at 10 months (**Figure 8A and B**). Since the PS1^{L166P} mutation
256 promotes APP cleavage, thereby increasing A β 42 production (Radde et al., 2006), we biochemically
257 quantified A β levels (**Figure 8-figure supplement 1A**) and performed histological measurements of
258 plaque loads using the 4G8 antibody that recognizes both human and murine A β (**Figure 8-figure**
259 **supplement 1B**). We also measured amyloid burden using Congo red to stain amyloid plaques, and OC
260 and A11 antibodies to recognize amyloid fibrils, fibrillary oligomers, and prefibrillar oligomers (Kayed et
261 al., 2007) in 19-month-old APPPS1 and APPPS1/HTT_{SA} mouse brains, a time that corresponds to the
262 final behavioral evaluation of the mice before histopathological analyses (**Figure 8-figure supplement**
263 **1C**). We found no significant differences between genotypes, indicating that loss of HTT phosphorylation
264 has no effect on A β level, amyloid load, A β oligomer load or plaque aggregation. These results indicate
265 that HTT dephosphorylation regulates presynaptic levels of APP^{Swe} without affecting downstream A β
266 production and/or accumulation.

267 We next quantified the number and the size of the spines in the CA1 region of 19-month-old mice by
268 electron microscopy. As previously described for APP^{Swe}-PS1^{ΔE9} mice, 5xFAD Tg mice, and APPxPS1-
269 Ki mice (Androuin et al., 2018; Koffie et al., 2009; Neuman et al., 2015), APPPS1 mice showed lower
270 synaptic density and larger spines than WT mice (**Figure 8C**). Strikingly, unphosphorylatable HTT
271 (HTT_{SA}) significantly increased spine density and completely rescued APPPS1-induced increase of spine
272 size (**Figure 8C**).

273

274 **Unphosphorylatable HTT improves learning and memory in APPPS1 mice**

275 We next investigated the behavior of WT, APPPS1, and APPPS1/HTT_{SA} mice. Extensive phenotypic
276 analysis of the HTT_{SA} mice using a modified SHIRPA primary screen and various behavioral tests
277 (**Figure 6-figure supplement 1 and table supplement 1**) revealed no significant changes in the
278 behavioral-neurological status of 12 to 15-month-old HTT_{SA} mice compared to WT mice. When we
279 compared WT, APPPS1, and APPPS1/HTT_{SA} mice, we found no significant differences in locomotor
280 activity or anxiety-related behavior in the open field test (**Figure 9-figure supplement 1**).

281 We then evaluated spatial learning of 12- to 15-month-old APPPS1 and APPPS1/HTT_{SA} mice in the
282 Morris water maze paradigm. As expected, APPPS1 mice took longer paths to reach the platform of the
283 water maze (**Figure 9A**). APPPS1/HTT_{SA} mice performed better than APPPS1 mice, although not to the
284 level of WT mice. Comparing the early and late stages of learning in the APPPS1/HTT_{SA} mice, we found
285 that APPPS1/HTT_{SA} mice performed about as poorly as the APPPS1 mice in the early stages of learning
286 (first training sessions). In the late training sessions, however, they performed much better than APPPS1
287 mice and showed a substantial recovery of performance (**Figure 9B**). Finally, we evaluated their memory
288 of the platform location by subjecting the mice to a probe trial. APPPS1 mice explored all quadrants of
289 the pool equally, whereas both WT and APPPS1/HTT_{SA} mice showed a preference for the target quadrant,
290 indicating that their memory of the platform was intact (**Figure 9C**).

291 We also subjected the mice to the Novel Object Recognition test (**Figure 9D**). APPPS1 mice spent
292 similar time investigating familiar and novel objects, indicating a memory deficit (indicated by a memory
293 index close to 50%). In contrast, APPPS1/HTT_{SA} mice behaved as WT mice and showed a marked
294 preference for the novel object (significantly different from the theoretical 50% random score), suggesting
295 that unphosphorylatable HTT can mitigate the memory deficit observed in APPPS1 mice.

296 We conclude that blocking Akt phosphorylation at HTT S421 reduces APP presynaptic levels,
297 improving learning and memory in APPPS1 mice.

298

299 **Discussion**

300 We used high-resolution live-cell imaging of isolated axonal and dendritic compartments in a mature
301 corticocortical network-on-a-chip to investigate the influence of HTT phosphorylation on APP trafficking.
302 We then evaluated the consequences of HTT phosphorylation on brain morphology and function in both
303 wild-type mice and in transgenic mice with AD-like neuropathology. We propose a model in which
304 axonal transport of APP, APP presynaptic levels, and synapse homeostasis require an intact Akt-HTT
305 pathway.

306

307 **HTT links APP axonal transport to presynaptic levels of APP**

308 We find that axonal, but not dendritic, transport of APP is regulated by Akt-phosphorylated HTT. We
309 previously showed that HTT phosphorylation at Serine 421 recruits kinesin-1 to the molecular motor
310 complex and promotes anterograde transport of vesicles to the plus end of microtubules in axons (Colin et
311 al., 2008). Given the mixed polarity of microtubules in dendrites (Kapitein and Hoogenraad, 2015; Yau et
312 al., 2016), modifying HTT phosphorylation affects APP transport only in axons, where all the
313 microtubules are oriented with the plus end towards the axon terminal. Our finding that the modulation of
314 axonal transport of APP regulates synaptic APP homeostasis is in agreement with nerve ligation studies,
315 which showed early on that blocking traffic from the entorhinal cortex to the dentate gyrus greatly
316 reduced APP levels at the synapse (Koo et al., 1990). Results obtained by pulse-chase labeling
317 experiments and unilateral lesions of the perforant path, a circuit by which axons from the entorhinal
318 cortex connect to the dentate gyrus, also accord with these results (Buxbaum et al., 1998; Lazarov et al.,
319 2002). Moreover, studies investigating the composition of APP vesicles report that most proteins co-
320 transported with APP are presynaptic (Kohli et al., 2012; Szodorai et al., 2009) and that APP colocalizes
321 with presynaptic proteins at the presynaptic bouton (Groemer et al., 2011). Notwithstanding the
322 contribution of dendritic APP to synapse homeostasis (Niederst et al., 2015), our results demonstrate that
323 APP levels at presynaptic membranes rely on HTT-dependent axonal transport.

324

325 **HTT phosphorylation, APP presynaptic levels and synapse homeostasis**

326 The absence of HTT phosphorylation reduced presynaptic levels of APP, restored synapse number
327 and PSD length, and attenuated memory deficits in APPS1 mice. In contrast, there was no effect of the
328 HTT S421A mutation on amyloid plaques, on different pools of A β oligomers, or on extracellular and
329 intracellular A β 42 levels in brain, although the existence of a pool of vesicular presynaptic A β has been
330 recently reported (Yu et al., 2018). These results suggest that HTT dephosphorylation regulates synapse
331 homeostasis by modulating presynaptic APP levels rather than modulating APP-derived A β production.
332 Notwithstanding the synaptic toxicity of A β peptides (Klementieva et al., 2017; Mucke and Selkoe, 2012;
333 Palop and Mucke, 2010; Selkoe and Hardy, 2016; Wei et al., 2010), our findings dovetail nicely with
334 previous results showing presynaptic APP contributes to synapse formation, function, and maintenance
335 (Hoe et al., 2012; Muller et al., 2017; Nicolas and Hassan, 2014).

336 Our results are also in accord with reports that *App* knockout increases the number of functional
337 synapses *in vitro* (Priller et al., 2006) and augments synaptic density *in vivo*, as visualized by two-photon
338 *in vivo* microscopy through a cranial window (Bittner et al., 2009). Indeed, we found that reducing APP
339 presynaptic levels by blocking HTT phosphorylation increases synapse density, and that this effect can be
340 reversed by over-expressing APP in presynaptic neurons. Conversely, and again in agreement with
341 previous studies (Alonso-Nanclares et al., 2013; Bittner et al., 2012; Priller et al., 2009), we found that

342 overexpressing APP and PS1 mutations *in vivo* reduced synaptic density, an effect that can be restored by
343 HTT-mediated reduction of APP presynaptic levels, without having significant effects on A β levels.
344 Although the precise physiological function of APP at the synapse remains to be elucidated, changes in
345 synapse homeostasis could be linked to the potential function of APP as an adhesion molecule that forms
346 homo and/or heteromeric complexes with APP family members (Muller et al., 2017; Soba et al., 2005).

347

348 **Relevance to disease pathogenesis**

349 Our identification of an Akt-HTT pathway that regulates APP and synapse homeostasis might be of
350 relevance for AD pathophysiology. Post-mortem analyses of AD patient brains report increased levels of
351 activated Akt in mid-temporal and mid-frontal cortex soluble fractions (Rickle et al., 2004) as well as
352 increased phosphorylation of Akt and of Akt substrates in membrane-bound fractions (Griffin et al., 2005).
353 Our finding that inhibiting Akt-mediated HTT phosphorylation reduces APP presynaptic levels in
354 APPPS1 mice suggests that increased Akt activity might contribute to higher presynaptic APP levels in
355 AD brains, leading to synapse loss and cognitive decline. Our findings may also relate to studies that
356 show rescue of synaptic and behavioral deficits in AD mouse models by knocking down the IGF-1
357 receptor and inhibiting the phosphoinositide 3 kinase (PI3K), which are upstream of Akt-HTT (Cohen et
358 al., 2009; Humbert et al., 2002; Martinez-Marmol et al., 2019). Prior to this study, the JNK-interacting
359 protein 1 (JIP1) was identified as a scaffold for APP (Muresan and Muresan, 2005). JIP1 determines the
360 directionality of APP trafficking through its phosphorylation at a JNK-dependent phosphorylation site (Fu
361 and Holzbaur, 2013) and could regulate amyloid-independent mechanisms of AD pathogenesis
362 (Margevicius et al., 2015). This study and ours highlight the complexity of the regulation of APP
363 trafficking in neurons, with different scaffolds (JNK and Akt) responding to specific signaling pathways.

364 Defects in APP trafficking could also contribute to synaptic defects observed in HD, as we found that
365 the Akt-HTT pathway is down-regulated in HD patient brain samples and lymphoblasts as well as in HD
366 rodent models (Colin et al., 2005; Humbert et al., 2002). Several studies have reported a notable reduction
367 in the number of synapses particularly within the corticostriatal circuit, which is the most profoundly
368 affected in HD (Virlogeux et al., 2018). A better understanding of HTT-APP relationships could help
369 unravel mechanisms of interest for both Huntington's disease and Alzheimer's disease.

370

371

372 **Contact for reagent and resource sharing**

373 Further information and requests for resources and reagents should be directed to and will be fulfilled by
374 the Lead Contact, Frédéric Saudou (Frederic.saudou@inserm.fr).

375

376 **Materials and methods**

377 **Mice**

378 The APP^{swe};PS1L166P (Tg Thy1-APPKM670/671NL;Thy1-PS1L166P referred as APPPS1) mouse
379 strain (#21; C57Bl6/J background) was obtained from Dr. M. Jucker's laboratory (Radde et al., 2006).
380 Heterozygous *Htt*^{S421A/+} Knock-In mice (C57Bl6/J background) were generated at the Mouse Clinical
381 Institute (Strasbourg, France) by introduction of a point mutation into Exon 9 (AGC>GCC, Ser>Ala) or
382 (AGC>GAC, Ser>Asp) concomitant with introduction of repeated regions LoxP_Neo_LoxP in intron 9
383 for genotyping and a FseI restriction site in intron 8 for cloning purpose. Homozygous *Htt*^{S421A/S421A}
384 Knock-In mice (HTT_{SA}) were generated and did not show obvious phenotype as shown previously (Thion
385 et al., 2015) and in this study. Transgenic APPPS1 mice in a *Htt*^{S421A/S421A} (HTT_{SA}) genetic background
386 mice were obtained by crossing homozygous *Htt*^{S421A/S421A} mice with transgenic APPPS1 mice thus
387 generating APPPS1;*Htt*^{S421A/+} mice that were crossed with heterozygous *Htt*^{S421A/+} mice to obtain
388 APPPS1;*Htt*^{S421A/S421A} mice, heretofore referred to as APPPS1/HTT_{SA} mice. WT mice used for
389 backcrossing and mouse amplification are C57Bl6/J mice from Charles River Laboratories (L'Arbresle,
390 France). WT mice used for behavioral and biochemical experiments are littermates of APPPS1/HTT_{SA}
391 and, of HTT_{SA} and APPPS1 mice respectively.

392 The general health of the mice was regularly checked and body weights were assessed weekly
393 throughout the experimental period. Animals were held in accordance with the French Animal Welfare
394 Act and the EU legislation (Council Directive 86/609/EEC) and the ARRIVE (Animal Research:
395 Reporting of In Vivo Experiments) guidelines. The French Ministry of Agriculture and the local ethics
396 committee gave specific authorization (authorization no. 04594.02) to BD to conduct the experiments
397 described in the present study.

398 To evaluate the effects of HTT_{SA} mutation on a wild-type background, a total of 23 mice were used.
399 To evaluate the effects of HTT_{SA} mutation on an APPPS1 transgenic background, a total of 84 mice were
400 used. Only male mice were studied, to avoid any potential effects of the estrus cycle on behavioral
401 responses. Behavioral phenotypes were analyzed between 12 and 15 months of age, a time at which
402 behavioral defects are observed in APPPS1 mice (Radde et al., 2006).

403

404 **Behavioral and Cognitive Evaluation**

405 The behavioral testing battery consisted of: primary modified SHIRPA screen (Rogers et al., 1997),
406 open field, elevated plus maze, novel object recognition, Morris water maze, and grip strength tests. All
407 tests were performed during light phases of the diurnal cycle. Mice were group housed (4-6/cage) and had
408 free access to food and water except during experiments. They were transported to the behavioral testing
409 room and allowed to acclimate for at least 1 h prior to initiating experiments.

410

411 *Novel Object Recognition test (NOR)*

412 The object recognition test is based on the natural tendency of rodents to spend more time
413 investigating a novel object than a familiar one (Ennaceur and Delacour, 1988). The choice to explore the
414 novel object reflects the use of recognition memory. Our protocol is similar to that previously described
415 (Scholtzova et al., 2009). The object recognition test was carried out in an illuminated (30 lux) square
416 gray PVC open field box (50 cm x 50 cm x 30 cm). The test consists of a familiarization session of 15
417 min in which mice explored the open field arena containing two identical, symmetrically placed objects
418 (A1 & A2). The following day, a training session of 15 min was run with two novel identical objects (B1
419 & B2). Retention was tested 3 h after the training session to evaluate object memory. During the retention
420 trial, mice were exposed to a third exemplar of the familiar object (B3) and to a novel object (C1) for 10
421 min. Behavioral monitoring was done with ANY-maze (Stoelting, USA). The results were expressed as a
422 recognition index, defined as percentage of the time spent exploring the new object over the total time
423 exploring the two objects. Experiments with animals whose exploration was not considered sufficient to
424 allow recognition (less than 6 s of exploration time during training and retention sessions) were discarded
425 from analysis.

426

427 *Morris Water Maze test (MWM)*

428 Spatial learning capacity was tested in the standard hidden-platform Morris water maze (MWM). The
429 maze consisted of a large circular pool (diameter 150 cm) filled with water to a depth of 35 cm. The
430 MWM protocol was adapted from a previous description (Lo et al., 2013). Briefly, mice were trained for
431 11 days to find a hidden platform (10 cm diameter) set at 1 cm beneath the surface of the water at a fixed
432 position in a selected, constant quadrant. The water was opacified with non-toxic white paint (ACUSOL,
433 Brenntag, Belgium) to prevent animals from seeing the platform. The water temperature was maintained
434 at 25-26°C with four thermostatically controlled heaters (Askoll Therm XL 200W, Truffaut, France). The
435 pool was situated at the center of a brightly lit room (~320 lux) with various fixed posters and visual cues
436 placed on the walls to act as distal landmarks. There were four trials per training day with an inter-trial
437 interval of 30 min. The mice were released into water at semi-randomly chosen cardinal compass points
438 (N, E, S, and W). Mice failing to reach the platform within 90 s were gently guided to the platform and

439 were left on it for 15 sec, before being dried and returned to their home cages. Two days of rest were
440 given after the 5th and 10th day of training. On the 11th day of training (i.e.: 72 h after last training
441 session), a probe trial was performed to evaluate robustness of spatial memory. During the probe trial, the
442 platform was removed and mice were released into the pool from the side diagonally opposite to where
443 the platform was located and allowed to swim freely for 90 s.

444 During all testing phases, a video camera was positioned above the pool for trial recording and the
445 ANY-maze videotracking software was used. Rather than measuring latency or distance traveled, which
446 could be biased by variations in swim speeds and path tortuosity, we analyzed the Corrected Integrated
447 Path Length (CIPL) (Gallagher et al., 1993) to assess learning during the 11 training days. During the
448 probe test the percent of time spent in each quadrant was assessed.

449

450 **Antibodies, plasmids and lentiviruses**

451 Antibodies used are anti-: HTT (clone D7F7, Cell Signaling; 5656), pHTT-S421 pAb 3517 (Colin et
452 al., 2008), GFP (for western blotting, Institut Curie, A-P-R#06), SNAP25 (AbCam, sb24737),
453 Synaptophysin (Cell Signaling; s5768), PSD95 (Millipore; mab1598), p38 (AbCam, ab14692), APP
454 (clone 22C11, Millipore; mab348), Lamin B1 (AbCam; ab133741), KHC (clone SUK4, Covance; MMS-
455 188P), p-150 (BD Transduction Laboratories, 610474), MAP-2 (Millipore; AB5622), GFP (for
456 Immunofluorescence experiments, AbCam; Ab13970), HA (clone 6E2, Cell Signaling, mAb#2367),
457 Tubulin (Sigma; t9026) and GAPDH (Sigma; G9545).

458 APP-mCherry (Marquer et al., 2014) plasmid was cloned into pSIN lentiviral vector (Drouet et al., 2009)
459 by Gateway system (Life Technology) using sense primer 5'-

460 GGGGACAAGTTTGTACAAAAAAGCAGGCTTCGAATTCTGCAGTCGACGG-3' and anti-sense
461 primer 5'-GGGGACCACTTTGTACAAGAAAGCTGGGTCGCGGCCGCCCTACTTGTACA-3' and
462 recombination. We verified whether APP-mCherry is cleaved in neuronal culture by endogenous

463 secretases but did not find aberrant cleavage of APP in our experimental conditions indicating that most
464 of the APP-containing vesicles correspond to full length APP (data not shown). Plasmids coding for
465 pHRIG-Akt1 (Akt-CA) and pHRIG-AktDN (Akt-N) were gifts from Heng Zhao (Addgene plasmids #
466 53583 and 53597 respectively). MAP2-GFP was previously described (Liot et al., 2013). Lentiviruses
467 encoding the first 480 amino acids of HTT with 17Q and with the S421A mutation have been previously
468 described (Pardo et al., 2006). Plasmid coding for GFP lentivector was a gift from Dr J. M. Heard.
469 Lentivectors were produced by the ENS Lyon Vectorology Facility with titer higher than 10^8 UI/ml.

470

471 **Vesicular transport imaging into microchambers**

472 Cortical neurons were isolated from mouse embryos (E15.5) according to Liot et al. 2013 (Liot et al.,

473 2013). Neurons were seeded on 12-well plate coated with poly-L-lysine (1 mg/ml) or into microchambers
474 coated with poly-D-lysine (0.1 mg/ml; presynaptic and synaptic compartments) or poly-D-lysine and
475 laminin 10 µg/ml (Sigma; postsynaptic compartment) and cultured at 37°C in a 5% CO₂ incubator for 13
476 days. For dendritic trafficking, mouse neurons were transfected before plating with 5 µg of MAP2-GFP
477 plasmid using a Nucleofector (Lonza) according to the manufacturer's specifications. After 8 days *in vitro*
478 (DIV8), neurons were transduced as previously described (Bruyere et al., 2015) into presynaptic neuron
479 chamber for axonal transport analysis or into the postsynaptic neuron chamber for the dendritic transport
480 analysis. Acquisitions were done at DIV13 on microgrooves, at the limit of the synaptic compartment, at
481 5 Hz for 1 min on inverted microscope (Axio Observer, Zeiss) coupled to a spinning-disk confocal system
482 (CSU-W1-T3; Yokogawa) connected to an electron-multiplying CCD (charge-coupled device) camera
483 (ProEM+1024, Princeton Instrument) at 37°C and 5% CO₂. Vesicle velocity, directional net flux and
484 vesicle number were measured on 100 µm of neurite using KymoTool Box ImageJ plugin as previously
485 described (Virlogeux et al., 2018). Vesicle velocity corresponds to segmental anterograde or retrograde
486 velocity. Directional net flux is the anterograde cumulative distance minus the retrograde cumulative
487 distance. Regarding vesicle number, a vesicle is considered anterograde when the distance travelled by
488 one vesicle is more anterograde than retrograde.

489

490 **Detection of active synapses**

491 Neurons were seeded into microfluidic devices and transduced at DIV1 with GFP lentivirus. The
492 synaptic chamber was incubated at indicated time with 10 µM of FM4-64 styryl dye (ThermoFischer
493 Scientific) into high KCl Tyrode solution (2 mM NaCl; 50 mM KCl; 2 mM CaCl₂; 1 mM MgCl₂; 10 mM
494 Glucose and 1 mM Hepes buffer pH7.4) during 1 min at 37°C. After 3 washes with Tyrode solution (150
495 mM NaCl; 4 mM KCl; 2 mM CaCl₂; 1 mM MgCl₂; 10 mM Glucose and 1 mM Hepes buffer pH7.4)
496 containing inhibitors of additional firing (1 mM kynurenic acid and 10 mM MgCl₂), acquisitions were
497 made on inverted microscope (Axio Observer, Zeiss) coupled to a spinning-disk confocal system (CSU-
498 W1-T3; Yokogawa) connected to an electron-multiplying CCD (charge-coupled device) camera
499 (ProEM+1024, Princeton Instrument) at 37°C and 5% CO₂ with z stacks of 5 µm.

500

501 **Quantification of exocytosis rate**

502 COS-1 cells were plated at low density on glass coverslips and transfected with APP-SEP (super
503 ecliptic pHluorin) and with pARIS HTT or pARIS HTT_{SA} (Pardo et al., 2010) using calcium phosphate.
504 Acquisitions were made the day after transfection at 5Hz during 1 min using an inverted microscope
505 (Elipse Ti, Nikon) with a X60 1.42 NA APO TIRF oil-immersion objective (Nikon) coupled to a CCD
506 camera (CoolSnap, Photometrics) and maintained at 37°C and 5% CO₂. Analysis was done on area

507 delimited by cell edges and exocytosis rate was quantified using ExocytosisAnalyser macro on ImageJ
508 developed by Marine Scoazec.

509

510 **Quantification of APP in the synaptic chamber**

511 Thirteen days after plating, media from synaptic or presynaptic compartments of 9 microchambres
512 per condition were removed. Lysis buffer containing 4 mM HEPES, pH 7.4, 320 mM sucrose and protease
513 inhibitor cocktail (Roche) mixed with 1X Laemmli buffer was added on synaptic and presynaptic
514 compartments during 30min. Harvested media containing lysed neurites and synapses were analyzed on
515 western blot.

516

517 **Fractionation of synaptosomes, PSD and non-PSD fractions**

518 Synaptosome purification was performed as previously described (Frändemiché et al., 2014). Cortex
519 was homogenized in cold buffer containing 4 mM HEPES, pH 7.4, 320 mM sucrose and protease inhibitor
520 cocktail (Roche). Homogenates were cleared at 1000 g for 10 min to remove nuclei and large debris. The
521 resulting supernatants were concentrated at 12,000 g for 20 min to obtain a crude membrane fraction,
522 which was then resuspended twice (4 mM HEPES, 1 mM EDTA, pH 7.4, 20 min at 12,000 g). Then, the
523 pellet was incubated (20 mM HEPES, 100 mM NaCl, 0.5% Triton X-100, pH 7.2) for 1h at 4°C with mild
524 agitation and centrifuged at 12,000 g for 20 min to pellet the synaptosomal membrane fraction. The
525 supernatant was collected as the non-postsynaptic density membrane fraction (non-PSD) or Triton-soluble
526 fraction. The pellet was then solubilized (20 mM HEPES, 0.15 mM NaCl, 1% Triton X-100, 1%
527 deoxycholic acid, 1% SDS, pH 7.5) for 1h at 4°C and centrifuged 15 min at 10,000 g. The supernatant
528 contained the PSD or Triton-insoluble fraction. The non-PSD integrity was checked by synaptophysin
529 immunoblotting and the PSD fraction was confirmed by the PSD-95 immunoblotting enriched in this
530 compartment.

531

532 **Synapse analysis by electron microscopy**

533 Mice were anaesthetized at 19 months of age with pentobarbital (120 mg/kg) and then transcardially
534 perfused with phosphate-buffer saline solution. Hippocampi were dissected and fixed with 2%
535 glutaraldehyde and 2% paraformaldehyde in 0.1 M phosphate buffer pH 7.2 during 48 hours at 4°C; the
536 CA1 area was dissected under the binocular and further fixed during 72 hours in the same solution.
537 Samples were then washed with buffer and post-fixed with 1% Osmium tetroxyde and 0.1 M phosphate
538 buffer pH 7.2 during 1 hour at 4°C. After extensive washing with water, cells were further stained with
539 1% uranyl acetate pH 4 in water during 1 hour at 4°C before being dehydrated through graded ethanol
540 (30%-60%-90%-100%-100%-100%) and infiltrate with a mix of 1/1 epon/alcohol 100% during 1 hour

541 and several bath of fresh epon (Flukka) during 3 hours. Finally, samples were included in a capsule full of
542 resin that was let to polymerize during 72 h at 60°C. Ultrathin sections of the samples were cut with an
543 ultramicrotome (Leica), sections were post-stained with 5% uranyl acetate and 0.4% lead citrate before
544 being observed with a transmission electron microscope at 80 kV (JEOL 1200EX). Images were acquired
545 with a digital camera (Veleta, SIS, Olympus) and morphometric analysis was performed with iTEM
546 software (Olympus). Quantification of synaptic density was done on axon-free neuropil regions (Zhang et
547 al., 2015).

548

549 **Immunostaining into microchambers**

550 Neurons within microchambers were fixed with a PFA/Sucrose solution (4%/4% in PBS) for 20 min
551 at room temperature (RT). The fixation buffer was rinsed three times with PBS and neurons were
552 incubated for 1h at RT with a blocking solution (BSA 1%, normal goat serum 2%, Triton X-100 0.1%).
553 For PSD95 and synaptophysin immunofluorescence, the synaptic compartment was then incubated
554 overnight at 4°C with primary antibodies PSD95 (Millipore, #MAB1598, 1:1,000) and Synaptophysin
555 (Abcam, #AB14692, 1:200). For GFP and MAP-2 immunofluorescence, all compartments were incubated
556 with primary antibodies against MAP-2 (Millipore; AB5622) and GFP (AbCam; Ab13970). After
557 washing with PBS, appropriate fluorescent secondary antibodies were incubated for 1h at RT. The
558 immunofluorescence was maintained in PBS for a maximum of one week in the dark at 4°C.
559 Immunostainings were acquired with a X63 oil-immersion objective (1.4 NA) using an inverted confocal
560 microscope (LSM 710, Zeiss) coupled to an Airyscan detector to improve signal-to-noise ratio and to
561 increase resolution. Juxtaposition analyses were performed using ImageJ. Airyscan images were
562 thresholded to remove non-specific signal and an area of interest of at least 100 µm in length was defined
563 around neurites. The number of synaptophysin spots overlapping, juxtaposed or separated by no more
564 than 2 pixels (130 nm) to PSD95 spots were counted manually. Results were expressed as a function of
565 neurite length and were normalized to 100 µm and WT condition. Each condition was tested using at least
566 2 chambers per culture from at least 2 independent cultures. In each chamber, 3 fields were analyzed in
567 which at least 3 regions of interest were selected (n = number of fields).

568

569 **MRI analyses**

570 *Brain preparation for ex vivo MRI acquisitions*

571 Skulls were processed as described in (Pagnamenta et al., 2019). Briefly, 4 male mice of each genotype
572 aged between 8 and 11 weeks were transcardially perfused with 4% paraformaldehyde solution in
573 phosphate buffered saline containing 6.25 mm of Gd-DOTA (Guerbet Laboratories, Roissy, France). This
574 contrast agent is added to reduce the MRI acquisition time. Skin and head muscles were removed to

575 expose the skull, which was then immersed in the fixing solution for 4 days. The skull was then
576 transferred to a Fomblin (FenS chemicals, Goes, Netherlands) bath for at least 7 days for the distribution
577 of Gd-DOTA to be homogeneous throughout the whole brain.

578

579 *MRI acquisitions*

580 Ex vivo 3D MRI acquisitions were performed as described in (Pagnamenta et al., 2019). Briefly, skulls
581 were put in a 9,4 T MRI (Bruker Biospec Avance III; IRMaGe facility) and a volume coil for
582 transmission and a head surface cryocoil for reception were used.

583 To quantify brain volume, the brain was segmented with a 3D T_{1W} gradient-echo MRI sequence
584 (repetition time: 35.2 ms, echo time: 8.5 ms, flip angle: 20 degrees, field of view: 12 x 9 x 18.1 mm³,
585 isotropic spatial resolution: 50 μm, 4 signal accumulations, total acquisition time per brain: 2 h 32 min).

586

587 *Quantitative analysis of brain volumes*

588 Quantitative analysis of brain volume was performed as described in (Pagnamenta et al., 2019). Briefly,
589 from 3D T_{1W} gradient-echo MRI images, brain structures were delimited manually with the help of Allen
590 mouse brain atlas (<http://atlas.brain-map.org/atlas>) every 5 slices by defining regions of interest (ROIs) on
591 the coronal orientation using Fiji software. Then, interpolation was applied using the segmentation editor
592 plug-in (http://fiji.sc/Segmentation_Editor) for the brain structures (total brain, cortex, hippocampus and
593 striatum) to be reconstructed. A color was attributed to each structure and its 3D reconstruction and
594 volume were determined using the Voxel counter plug-in in the Fiji software

595 (https://imagej.net/3D_Viewer). Volume was calculated as following: number of voxels x voxel volume.

596 All segmentations were done blind to the genotype. Mann and Whitney test was used for comparison.

597

598 **Statistical analyses**

599 All cellular biology experiments were repeated in at least in three different batches of cultures.

600 Normality of data distribution was verified by graphical analysis of the data distribution and residues. For

601 data with assumed normal distribution, groups were compared by parametric tests followed by post hoc

602 analyses for multiple comparisons. Non-parametric tests were used for Western blot analyses and Aβ

603 dosages. *p < 0.05; **p < 0.01; ***p < 0.001; ****p < 0.0001; ns, not significant. Statistical calculations

604 were performed using GraphPad Prism 6.0.

605

606 **Acknowledgements**

607 We thank Luc Buée, Alain Buisson, Subhojit Roy, Rémy Sadoul, and members of the Saudou,
608 Humbert and Potier labs for comments; Vicky Brandt for critical reading; Caroline Benstaali, Anne
609 Bertrand, Camille Brochier, Aurélie Genoux, Félicie Lorenc, Jessica Roland, Chiara Scaramuzzino,
610 Marine Scoazec and Gisela Zalcmann for technical help and/or initial experiments; Daniel Choquet for
611 the gift of Super-Ecliptic-pHluorin-APP plasmid, Y. Saoudi and the GIN imaging facility (PIC-GIN) for
612 help with image acquisitions; G. Froment, D. Nègre, and C. Costa from SFR Biosciences
613 (UMS3444/CNRS, US8/Inserm, ENS de Lyon, UCBL) for lentivirus production; Emmanuel Barbier and
614 Olivier Montigon (UMS 3552/US17 IRMage) for MRI acquisitions; the technical staff of the
615 PHENOPARC platform and the HISTOMICS platform of the ICM for behavioral and histological
616 studies. This work was supported by grants from Agence Nationale de la Recherche: ANR-12-MALZ-
617 0004 HuntAbeta, F.S. and M.C.P.; ANR-14-CE35-0027-01 PASSAGE, F.S.; ANR-15-IDEX-02
618 NeuroCoG (F.S.) and ANR-10-IAIHU-06 (M.C.P.) in the framework of the “Investissements d’avenir”
619 program), Fondation pour la Recherche Médicale (FRM, DEI20151234418, F.S.; DEQ20170336752,
620 S.H.), Fondation pour la Recherche sur le Cerveau (FRC)(F.S.), Fondation Bettencourt Schueller (F.S.)
621 and AGEMED program from INSERM (F.S. & S.H.). IRMaGe is partly funded by “Investissements
622 d’Avenir” run by the French National Research Agency, grant “Infrastructure d’avenir en Biologie Santé”
623 (ANR-11-INBS-0006). F.S. laboratory is member of the Grenoble Center of Excellence in
624 Neurodegeneration (GREEN). H.V. was supported by a PhD fellowship from Association Huntington
625 France. F.S. laboratory is member of the Grenoble Center of Excellence in Neurodegeneration (GREEN).

626

627 **Author contributions**

628 Conceptualization, J.B., S.H., M.C.P., B.D. and F.S.; Formal Analysis, J.B., Y.A., H.V., J.C.D., E.D. and
629 K.P.G; Investigation, J.B., Y.A., H.V., G.F., J.C.D., A.C., C.B. and K.P.G; Methodology, J.B., Y.A., H.V.,
630 J.C.D., E.D., S.H., M.C.P., B.D., and F.S.; Visualization, J.B., Y.A., H.V., J.C.D., E.D., K.P.G., B.D.,
631 and F.S; Writing – Original Draft, J.B., Y.A., M.C.P., B.D., and F.S.; Writing - Review & Editing, J.B.,
632 Y.A., H.V., A.A., S.H., M.C.P., B.D., and F.S.; Supervision, A.A., S.H., M.C.P., B.D. and F.S.; Project
633 administration, F.S., Funding Acquisition, M.C.P. and F.S.

634

635 **Additional information**

636 **Supplementary files** include 5 Supplementary Figures, 1 Supplementary Table and 5 Supplementary
637 Movies and 1 data source document.

638

639 **Competing financial interests:**

640 F.S. is on the scientific advisory board of Servier (Neurosciences Department) and a consultant for TEVA
641 and Wave Life Sciences. The other authors declare that they have no competing interests.

642

643 **References**

644 Alonso-Nanclares, L., Merino-Serrais, P., Gonzalez, S., and DeFelipe, J. (2013). Synaptic changes in the
645 dentate gyrus of APP/PS1 transgenic mice revealed by electron microscopy. *J Neuropathol Exp Neurol* 72,
646 386-395.

647 Androuin, A., Potier, B., Nagerl, U.V., Cattaert, D., Danglot, L., Thierry, M., Youssef, I., Triller, A.,
648 Duyckaerts, C., El Hachimi, K.H., *et al.* (2018). Evidence for altered dendritic spine
649 compartmentalization in Alzheimer's disease and functional effects in a mouse model. *Acta Neuropathol*
650 135, 839-854.

651 Bittner, T., Burgold, S., Dorostkar, M.M., Fuhrmann, M., Wegenast-Braun, B.M., Schmidt, B.,
652 Kretzschmar, H., and Herms, J. (2012). Amyloid plaque formation precedes dendritic spine loss. *Acta*
653 *Neuropathol* 124, 797-807.

654 Bittner, T., Fuhrmann, M., Burgold, S., Jung, C.K., Volbracht, C., Steiner, H., Mitteregger, G.,
655 Kretzschmar, H.A., Haass, C., and Herms, J. (2009). Gamma-secretase inhibition reduces spine density in
656 vivo via an amyloid precursor protein-dependent pathway. *J Neurosci* 29, 10405-10409.

657 Brunholz, S., Sisodia, S., Lorenzo, A., Deyts, C., Kins, S., and Morfini, G. (2011). Axonal transport of
658 APP and the spatial regulation of APP cleavage and function in neuronal cells. *Experimental Brain*
659 *Research*, 1-12.

660 Bruyere, J., Roy, E., Ausseil, J., Lemonnier, T., Teyre, G., Bohl, D., Etienne-Manneville, S., Lortat-Jacob,
661 H., Heard, J.M., and Vitry, S. (2015). Heparan sulfate saccharides modify focal adhesions: implication in
662 mucopolysaccharidosis neuropathophysiology. *J Mol Biol* 427, 775-791.

663 Buggia-Prevot, V., Fernandez, C.G., Riordan, S., Vetrivel, K.S., Roseman, J., Waters, J., Bindokas, V.P.,
664 Vassar, R., and Thinakaran, G. (2014). Axonal BACE1 dynamics and targeting in hippocampal neurons: a
665 role for Rab11 GTPase. *Mol Neurodegener* 9, 1.

666 Buxbaum, J.D., Thinakaran, G., Koliatsos, V., O'Callahan, J., Slunt, H.H., Price, D.L., and Sisodia, S.S.
667 (1998). Alzheimer amyloid protein precursor in the rat hippocampus: transport and processing through the
668 perforant path. *J Neurosci* 18, 9629-9637.

669 Cohen, E., Paulsson, J.F., Blinder, P., Burstyn-Cohen, T., Du, D., Estepa, G., Adame, A., Pham, H.M.,
670 Holzenberger, M., Kelly, J.W., *et al.* (2009). Reduced IGF-1 signaling delays age-associated
671 proteotoxicity in mice. *Cell* 139, 1157-1169.

672 Colin, E., Regulier, E., Perrin, V., Durr, A., Brice, A., Aebischer, P., Deglon, N., Humbert, S., and
673 Saudou, F. (2005). Akt is altered in an animal model of Huntington's disease and in patients. *Eur J*
674 *Neurosci* 21, 1478-1488.

675 Colin, E., Zala, D., Liot, G., Rangone, H., Borrell-Pages, M., Li, X.J., Saudou, F., and Humbert, S. (2008).
676 Huntingtin phosphorylation acts as a molecular switch for anterograde/retrograde transport in neurons.
677 *Embo J* 27, 2124-2134.

678 Das, U., Wang, L., Ganguly, A., Saikia, J.M., Wagner, S.L., Koo, E.H., and Roy, S. (2016). Visualizing
679 APP and BACE-1 approximation in neurons yields insight into the amyloidogenic pathway. *Nat Neurosci*
680 19, 55-64.

681 Drouet, V., Perrin, V., Hassig, R., Dufour, N., Auregan, G., Alves, S., Bonvento, G., Brouillet, E., Luthi-
682 Carter, R., Hantraye, P., *et al.* (2009). Sustained effects of nonallele-specific Huntingtin silencing. *Ann*
683 *Neurol* 65, 276-285.

684 Ehinger, Y., Bruyere, J., Panayotis, N., Abada, Y.S., Borloz, E., Matagne, V., Scaramuzzino, C., Vitet, H.,
685 Delatour, B., Saidi, L., *et al.* (2020). Huntingtin phosphorylation governs BDNF homeostasis and
686 improves the phenotype of *Mecp2* knockout mice. *EMBO Mol Med*, e10889.

687 Ennaceur, A., and Delacour, J. (1988). A new one-trial test for neurobiological studies of memory in rats.
688 1: Behavioral data. *Behav Brain Res* 31, 47-59.

689 Fanutza, T., Del Prete, D., Ford, M.J., Castillo, P.E., and D'Adamio, L. (2015). APP and APLP2 interact
690 with the synaptic release machinery and facilitate transmitter release at hippocampal synapses. *Elife* 4,
691 e09743.

692 Frandemiche, M.L., De Seranno, S., Rush, T., Borel, E., Elie, A., Arnal, I., Lante, F., and Buisson, A.
693 (2014). Activity-dependent tau protein translocation to excitatory synapse is disrupted by exposure to
694 amyloid-beta oligomers. *J Neurosci* 34, 6084-6097.

695 Fu, M.M., and Holzbaur, E.L. (2013). JIP1 regulates the directionality of APP axonal transport by
696 coordinating kinesin and dynein motors. *J Cell Biol* 202, 495-508.

697 Gallagher, M., Burwell, R., and Burchinal, M. (1993). Severity of spatial learning impairment in aging:
698 development of a learning index for performance in the Morris water maze. *Behav Neurosci* 107, 618-626.

699 Gibbs, K.L., Greensmith, L., and Schiavo, G. (2015). Regulation of Axonal Transport by Protein Kinases.
700 *Trends Biochem Sci* 40, 597-610.

701 Griffin, R.J., Moloney, A., Kelliher, M., Johnston, J.A., Ravid, R., Dockery, P., O'Connor, R., and O'Neill,
702 C. (2005). Activation of Akt/PKB, increased phosphorylation of Akt substrates and loss and altered
703 distribution of Akt and PTEN are features of Alzheimer's disease pathology. *J Neurochem* 93, 105-117.

704 Groemer, T.W., Thiel, C.S., Holt, M., Riedel, D., Hua, Y., Huve, J., Wilhelm, B.G., and Klingauf, J.
705 (2011). Amyloid precursor protein is trafficked and secreted via synaptic vesicles. *PLoS One* 6, e18754.

706 Her, L.S., and Goldstein, L.S. (2008). Enhanced sensitivity of striatal neurons to axonal transport defects
707 induced by mutant huntingtin. *J Neurosci* 28, 13662-13672.

708 Hoe, H.S., Lee, H.K., and Pak, D.T. (2012). The upside of APP at synapses. *CNS Neurosci Ther* 18, 47-
709 56.

710 Humbert, S., Bryson, E.A., Cordelieres, F.P., Connors, N.C., Datta, S.R., Finkbeiner, S., Greenberg, M.E.,
711 and Saudou, F. (2002). The IGF-1/Akt pathway is neuroprotective in Huntington's disease and involves
712 Huntingtin phosphorylation by Akt. *Dev Cell* 2, 831-837.

713 Kaether, C., Skehel, P., and Dotti, C.G. (2000). Axonal membrane proteins are transported in distinct
714 carriers: a two-color video microscopy study in cultured hippocampal neurons. *Mol Biol Cell* 11, 1213-
715 1224.

716 Kapitein, L.C., and Hoogenraad, C.C. (2015). Building the Neuronal Microtubule Cytoskeleton. *Neuron*
717 87, 492-506.

718 Kaye, R., Head, E., Sarsoza, F., Saing, T., Cotman, C.W., Necula, M., Margol, L., Wu, J., Breydo, L.,
719 Thompson, J.L., *et al.* (2007). Fibril specific, conformation dependent antibodies recognize a generic
720 epitope common to amyloid fibrils and fibrillar oligomers that is absent in prefibrillar oligomers. *Mol*
721 *Neurodegener* 2, 18.

722 Klementieva, O., Willen, K., Martinsson, I., Israelsson, B., Engdahl, A., Cladera, J., Uvdal, P., and
723 Gouras, G.K. (2017). Pre-plaque conformational changes in Alzheimer's disease-linked Abeta and APP.
724 *Nat Commun* 8, 14726.

725 Klevanski, M., Herrmann, U., Weyer, S.W., Fol, R., Cartier, N., Wolfer, D.P., Caldwell, J.H., Korte, M.,
726 and Muller, U.C. (2015). The APP Intracellular Domain Is Required for Normal Synaptic Morphology,
727 Synaptic Plasticity, and Hippocampus-Dependent Behavior. *J Neurosci* 35, 16018-16033.

728 Koffie, R.M., Meyer-Luehmann, M., Hashimoto, T., Adams, K.W., Mielke, M.L., Garcia-Alloza, M.,
729 Micheva, K.D., Smith, S.J., Kim, M.L., Lee, V.M., *et al.* (2009). Oligomeric amyloid beta associates with
730 postsynaptic densities and correlates with excitatory synapse loss near senile plaques. *Proc Natl Acad Sci*
731 *U S A* 106, 4012-4017.

732 Kohli, B.M., Pflieger, D., Mueller, L.N., Carbonetti, G., Aebbersold, R., Nitsch, R.M., and Konietzko, U.
733 (2012). Interactome of the amyloid precursor protein APP in brain reveals a protein network involved in
734 synaptic vesicle turnover and a close association with Synaptotagmin-1. *J Proteome Res* 11, 4075-4090.

735 Koo, E.H., Sisodia, S.S., Archer, D.R., Martin, L.J., Weidemann, A., Beyreuther, K., Fischer, P., Masters,
736 C.L., and Price, D.L. (1990). Precursor of amyloid protein in Alzheimer disease undergoes fast
737 anterograde axonal transport. *Proc Natl Acad Sci U S A* 87, 1561-1565.

738 Lazarov, O., Lee, M., Peterson, D.A., and Sisodia, S.S. (2002). Evidence that synaptically released beta-
739 amyloid accumulates as extracellular deposits in the hippocampus of transgenic mice. *J Neurosci* 22,
740 9785-9793.

741 Liot, G., Zala, D., Pla, P., Mottet, G., Piel, M., and Saudou, F. (2013). Mutant Huntingtin alters retrograde
742 transport of TrkB receptors in striatal dendrites. *J Neurosci* 33, 6298-6309.

743 Lo, A.C., Tesseur, I., Scopes, D.I., Nerou, E., Callaerts-Vegh, Z., Vermaercke, B., Treherne, J.M., De
744 Strooper, B., and D'Hooge, R. (2013). Dose-dependent improvements in learning and memory deficits in
745 APPPS1-21 transgenic mice treated with the orally active Abeta toxicity inhibitor SEN1500.
746 *Neuropharmacology* 75, 458-466.

747 Margevicius, D.R., Bastian, C., Fan, Q., Davis, R.J., and Pimplikar, S.W. (2015). JNK-interacting protein
748 1 mediates Alzheimer's-like pathological features in AICD-transgenic mice. *Neurobiol Aging* 36, 2370-
749 2379.

750 Marquer, C., Laine, J., Dauphinot, L., Hanbouch, L., Lemercier-Neuillet, C., Pierrot, N., Bossers, K., Le,
751 M., Corlier, F., Benstaali, C., *et al.* (2014). Increasing membrane cholesterol of neurons in culture
752 recapitulates Alzheimer's disease early phenotypes. *Mol Neurodegener* 9, 60.

753 Martinez-Marmol, R., Mohannak, N., Qian, L., Wang, T., Gormal, R.S., Ruitenber, M.J.,
754 Vanhaesebroeck, B., Coulson, E.J., and Meunier, F.A. (2019). p110delta PI3-Kinase Inhibition Perturbs
755 APP and TNFalpha Trafficking, Reduces Plaque Burden, Dampens Neuroinflammation, and Prevents
756 Cognitive Decline in an Alzheimer's Disease Mouse Model. *J Neurosci* 39, 7976-7991.

757 Matsuda, S., Yasukawa, T., Homma, Y., Ito, Y., Niikura, T., Hiraki, T., Hirai, S., Ohno, S., Kita, Y.,
758 Kawasumi, M., *et al.* (2001). c-Jun N-terminal kinase (JNK)-interacting protein-1b/islet-brain-1 scaffolds
759 Alzheimer's amyloid precursor protein with JNK. *J Neurosci* 21, 6597-6607.

760 Moutaux, E., Christaller, W., Scaramuzzino, C., Genoux, A., Charlot, B., Cazorla, M., and Saudou, F.
761 (2018). Neuronal network maturation differently affects secretory vesicles and mitochondria transport in
762 axons. *Sci Rep* 8, 13429.

763 Mucke, L., and Selkoe, D.J. (2012). Neurotoxicity of amyloid beta-protein: synaptic and network
764 dysfunction. *Cold Spring Harb Perspect Med* 2, a006338.

765 Muller, U.C., Deller, T., and Korte, M. (2017). Not just amyloid: physiological functions of the amyloid
766 precursor protein family. *Nat Rev Neurosci* 18, 281-298.

767 Muresan, Z., and Muresan, V. (2005). Coordinated transport of phosphorylated amyloid-beta precursor
768 protein and c-Jun NH2-terminal kinase-interacting protein-1. *J Cell Biol* 171, 615-625.

769 Neuman, K.M., Molina-Campos, E., Musial, T.F., Price, A.L., Oh, K.J., Wolke, M.L., Buss, E.W., Scheff,
770 S.W., Mufson, E.J., and Nicholson, D.A. (2015). Evidence for Alzheimer's disease-linked synapse loss

771 and compensation in mouse and human hippocampal CA1 pyramidal neurons. *Brain Struct Funct* 220,
772 3143-3165.

773 Nicolas, M., and Hassan, B.A. (2014). Amyloid precursor protein and neural development. *Development*
774 141, 2543-2548.

775 Niederst, E.D., Reyna, S.M., and Goldstein, L.S. (2015). Axonal amyloid precursor protein and its
776 fragments undergo somatodendritic endocytosis and processing. *Mol Biol Cell* 26, 205-217.

777 Pagnamenta, A.T., Heemeryck, P., Martin, H.C., Bosc, C., Peris, L., Uszynski, I., Gory-Faure, S., Couly,
778 S., Deshpande, C., Siddiqui, A., *et al.* (2019). Defective tubulin detyrosination causes structural brain
779 abnormalities with cognitive deficiency in humans and mice. *Hum Mol Genet* 28, 3391-3405.

780 Palop, J.J., and Mucke, L. (2010). Amyloid-beta-induced neuronal dysfunction in Alzheimer's disease:
781 from synapses toward neural networks. *Nat Neurosci* 13, 812-818.

782 Pardo, R., Colin, E., Regulier, E., Aebischer, P., Deglon, N., Humbert, S., and Saudou, F. (2006).
783 Inhibition of calcineurin by FK506 protects against polyglutamine-huntingtin toxicity through an increase
784 of huntingtin phosphorylation at S421. *J Neurosci* 26, 1635-1645.

785 Pardo, R., Molina-Calavita, M., Poizat, G., Keryer, G., Humbert, S., and Saudou, F. (2010). pARIS-htt:
786 an optimised expression platform to study huntingtin reveals functional domains required for vesicular
787 trafficking. *Mol Brain* 3, 17.

788 Priller, C., Bauer, T., Mitteregger, G., Krebs, B., Kretzschmar, H.A., and Herms, J. (2006). Synapse
789 formation and function is modulated by the amyloid precursor protein. *J Neurosci* 26, 7212-7221.

790 Priller, C., Mitteregger, G., Paluch, S., Vassallo, N., Staufenbiel, M., Kretzschmar, H.A., Jucker, M., and
791 Herms, J. (2009). Excitatory synaptic transmission is depressed in cultured hippocampal neurons of
792 APP/PS1 mice. *Neurobiol Aging* 30, 1227-1237.

793 Radde, R., Bolmont, T., Kaeser, S.A., Coomaraswamy, J., Lindau, D., Stoltze, L., Calhoun, M.E., Jaggi,
794 F., Wolburg, H., Gengler, S., *et al.* (2006). Abeta42-driven cerebral amyloidosis in transgenic mice
795 reveals early and robust pathology. *EMBO Rep* 7, 940-946.

796 Rickle, A., Bogdanovic, N., Volkman, I., Winblad, B., Ravid, R., and Cowburn, R.F. (2004). Akt activity
797 in Alzheimer's disease and other neurodegenerative disorders. *Neuroreport* 15, 955-959.

798 Rodrigues, E.M., Weissmiller, A.M., and Goldstein, L.S. (2012). Enhanced beta-secretase processing
799 alters APP axonal transport and leads to axonal defects. *Hum Mol Genet* 21, 4587-4601.

800 Rogers, D.C., Fisher, E.M., Brown, S.D., Peters, J., Hunter, A.J., and Martin, J.E. (1997). Behavioral and
801 functional analysis of mouse phenotype: SHIRPA, a proposed protocol for comprehensive phenotype
802 assessment. *Mamm Genome* 8, 711-713.

803 Saudou, F., and Humbert, S. (2016). The Biology of Huntingtin. *Neuron* 89, 910-926.

804 Scholtzova, H., Kasczak, R.J., Bates, K.A., Boutajangout, A., Kerr, D.J., Meeker, H.C., Mehta, P.D.,
805 Spinner, D.S., and Wisniewski, T. (2009). Induction of toll-like receptor 9 signaling as a method for
806 ameliorating Alzheimer's disease-related pathology. *J Neurosci* 29, 1846-1854.

807 Selkoe, D.J., and Hardy, J. (2016). The amyloid hypothesis of Alzheimer's disease at 25 years. *EMBO*
808 *Mol Med* 8, 595-608.

809 Soba, P., Eggert, S., Wagner, K., Zentgraf, H., Siehl, K., Kreger, S., Lower, A., Langer, A., Merdes, G.,
810 Paro, R., *et al.* (2005). Homo- and heterodimerization of APP family members promotes intercellular
811 adhesion. *EMBO J* 24, 3624-3634.

812 Sudhof, T.C. (2018). Towards an Understanding of Synapse Formation. *Neuron* 100, 276-293.

813 Szodorai, A., Kuan, Y.H., Hunzelmann, S., Engel, U., Sakane, A., Sasaki, T., Takai, Y., Kirsch, J., Muller,
814 U., Beyreuther, K., *et al.* (2009). APP anterograde transport requires Rab3A GTPase activity for assembly
815 of the transport vesicle. *J Neurosci* 29, 14534-14544.

816 Takemura, R., Okabe, S., Umeyama, T., and Hirokawa, N. (1995). Polarity orientation and assembly
817 process of microtubule bundles in nocodazole-treated, MAP2c-transfected COS cells. *Mol Biol Cell* 6,
818 981-996.

819 Taylor, A.M., Blurton-Jones, M., Rhee, S.W., Cribbs, D.H., Cotman, C.W., and Jeon, N.L. (2005). A
820 microfluidic culture platform for CNS axonal injury, regeneration and transport. *Nat Methods* 2, 599-605.

821 Taylor, A.M., Dieterich, D.C., Ito, H.T., Kim, S.A., and Schuman, E.M. (2010). Microfluidic local
822 perfusion chambers for the visualization and manipulation of synapses. *Neuron* 66, 57-68.

823 Thion, M.S., McGuire, J.R., Sousa, C.M., Fuhrmann, L., Fitamant, J., Leboucher, S., Vacher, S., du
824 Montcel, S.T., Bieche, I., Bernet, A., *et al.* (2015). Unraveling the Role of Huntingtin in Breast Cancer
825 Metastasis. *J Natl Cancer Inst* 107.

826 Toh, W.H., and Gleeson, P.A. (2016). Dysregulation of intracellular trafficking and endosomal sorting in
827 Alzheimer's disease: controversies and unanswered questions. *Biochem J* 473, 1977-1993.

828 Vagnoni, A., Glennon, E.B., Perkinton, M.S., Gray, E.H., Noble, W., and Miller, C.C. (2013). Loss of c-
829 Jun N-terminal kinase-interacting protein-1 does not affect axonal transport of the amyloid precursor
830 protein or Abeta production. *Hum Mol Genet* 22, 4646-4652.

831 van Beuningen, S.F., and Hoogenraad, C.C. (2016). Neuronal polarity: remodeling microtubule
832 organization. *Curr Opin Neurobiol* 39, 1-7.

833 Verhey, K.J., Meyer, D., Deehan, R., Blenis, J., Schnapp, B.J., Rapoport, T.A., and Margolis, B. (2001).
834 Cargo of kinesin identified as JIP scaffolding proteins and associated signaling molecules. *J Cell Biol* 152,
835 959-970.

836 Virlogeux, A., Moutaux, E., Christaller, W., Genoux, A., Bruyere, J., Fino, E., Charlot, B., Cazorla, M.,
837 and Saudou, F. (2018). Reconstituting Corticostriatal Network on-a-Chip Reveals the Contribution of the
838 Presynaptic Compartment to Huntington's Disease. *Cell Rep* 22, 110-122.

839 Wei, W., Nguyen, L.N., Kessels, H.W., Hagiwara, H., Sisodia, S., and Malinow, R. (2010). Amyloid beta
840 from axons and dendrites reduces local spine number and plasticity. *Nat Neurosci* 13, 190-196.

841 Weyer, S.W., Zagrebelsky, M., Herrmann, U., Hick, M., Ganss, L., Gobbert, J., Gruber, M., Altmann, C.,
842 Korte, M., Deller, T., *et al.* (2014). Comparative analysis of single and combined APP/APLP knockouts
843 reveals reduced spine density in APP-KO mice that is prevented by APP α expression. *Acta*
844 *Neuropathol Commun* 2, 36.

845 Yau, K.W., Schatzle, P., Tortosa, E., Pages, S., Holtmaat, A., Kapitein, L.C., and Hoogenraad, C.C.
846 (2016). Dendrites In Vitro and In Vivo Contain Microtubules of Opposite Polarity and Axon Formation
847 Correlates with Uniform Plus-End-Out Microtubule Orientation. *J Neurosci* 36, 1071-1085.

848 Yu, Y., Jans, D.C., Winblad, B., Tjernberg, L.O., and Schedin-Weiss, S. (2018). Neuronal A β 42 is
849 enriched in small vesicles at the presynaptic side of synapses. *Life Science Alliance* 1, e201800028.

850 Zhang, Z., Song, M., Liu, X., Su Kang, S., Duong, D.M., Seyfried, N.T., Cao, X., Cheng, L., Sun, Y.E.,
851 Ping Yu, S., *et al.* (2015). Delta-secretase cleaves amyloid precursor protein and regulates the
852 pathogenesis in Alzheimer's disease. *Nat Commun* 6, 8762.

853 Zou, C., Montagna, E., Shi, Y., Peters, F., Blazquez-Llorca, L., Shi, S., Filser, S., Dorostkar, M.M., and
854 Herms, J. (2015). Intraneuronal APP and extracellular Abeta independently cause dendritic spine
855 pathology in transgenic mouse models of Alzheimer's disease. *Acta Neuropathol* 129, 909-920.

856

857 **Figure 1. Reconstituted corticocortical mature neuronal circuit**

858 (A) Image and schematic representation of the 3-compartment microfluidic chamber that allows the
859 reconstitution of a corticocortical mature network compatible with live-cell imaging of axons and
860 dendrites. (B) Presynaptic neurons were transduced with GFP (green) to visualize axons into
861 microgrooves and MAP2 (red) immunostaining was applied on the entire microchamber at DIV13.
862 Magnification shows axons into distal part of long microchannel but not MAP2-positive dendrites (C)
863 Functional synapses were detected using FM4-64 dye (purple) that labels active presynaptic boutons on
864 GFP dendrites (green) upon 50 mM KCl stimulation. Images represent a projection of 5 μ m Z stacks. The
865 highest number of functional corticocortical synapses is visualized between DIV10 and DIV15 in this
866 microfluidic device. Scale bar = 20 μ m.

867 **Figure supplement 1.** Time course of kinetics of anterograde and retrograde APP-mCherry axonal
868 velocity after plating neurons into microchambers.

869

870 **Figure 2. Transport of APP in axons and dendrites in reconstituted corticocortical mature neuronal**
871 **circuit.**

872 (A) APP-mCherry was transduced into the presynaptic compartment for axonal transport analysis or into
873 the postsynaptic compartment for dendritic trafficking. Postsynaptic neurons were transfected with MAP-
874 2-GFP (green) to visualize dendrites that cross the short microchannels. APP-mCherry transport along the
875 axons or the dendrites are represented in time projections of maximum signal intensities for 60 seconds
876 (middle panels) and real time-lapse analysis of anterograde/retrograde or inward/outward vesicles in
877 axons and dendrites respectively (right panel). Scale bars = 20 μ m. (B) Kymograph analyses of APP-
878 mCherry axonal or dendritic transport at DIV13 from time-lapse images acquired every 200 ms during 60
879 seconds. Transport characteristics such as the anterograde/retrograde or inward/outward vesicle velocities,
880 moving vesicle number per 100 μ m of neurite length, the cumulative distances travelled by vesicles and
881 thus the directional net flux of APP-mCherry trafficking into axons (upper panel) or dendrites (lower
882 panel) are represented by means \pm SEM of 3 independent experiments, 40 axonal and 120 dendritic
883 axons and 674 axonal and 1160 dendritic vesicles. Scale bars = 20 μ m. (see also Video 1 and 2)

884

885 **Figure 3. Axonal but not dendritic transport of APP depends on HTT phosphorylation.**

886 (A) Kymographs and quantifications of APP-mCherry into WT, HTT_{SA} and HTT_{SD} axons. Velocity,
887 vesicle number per 100 μ m of neurite length, cumulative distance and directional net flux were measured.
888 Histograms represent means \pm SEM of 3 independent experiments, 41 WT, 52 HTT_{SA} and 63 HTT_{SD}
889 axons and 674 WT, 602 HTT_{SA} and 493 HTT_{SD} vesicles. Significance was determined using an unpaired
890 t-test; * p < 0.05, ** p < 0.01, *** p < 0.001, **** p < 0.0001, ns = not significant. Scale bar = 20 μ m.

891 **(B)** Kymographs and quantifications of APP-mCherry into WT, HTT_{SA} and HTT_{SD} dendrites. Dendritic
892 inward and outward velocity, vesicle number per 100µm of neurite length, cumulative distance and
893 directional net flux were measured. Histograms represent means +/- SEM of 4 independent experiments,
894 122 WT, 99 HTT_{SA} and 109 HTT_{SD} dendrites, 1171 WT, 1119 HTT_{SA} and 1074 HTT_{SD} vesicles.
895 Significance was determined using an unpaired t-test; * p < 0.05; ns = not significant. Scale bar = 20 µm.
896 (see also Video 3).

897 **Figure supplement 1.** Vesicular distribution of kinesin and dynactin in WT and HTT_{SA} mouse brains

898

899 **Figure 4 Akt regulates APP transport in a HTT phospho-dependent manner.**

900 **(A)** WT and HTT_{SA} neurons transduced with constitutively active Akt (Akt-CA GFP) or an inactive form
901 of Akt (Akt-N GFP) in IRES GFP constructs or with empty GFP vector (GFP) were analyzed by western
902 blotting with Akt, GFP, phosphorylated HTT, total HTT and tubulin antibodies. **(B)** Kymographs of APP-
903 mCherry from WT and HTT_{SA} neurons seeded in microchambers and transduced with APP-mCherry and
904 GFP, Akt-CA GFP or Akt-N GFP. Scale bar 20µm. (see also Video 4). **(C)** Velocity and directional net
905 flux of APP-mCherry vesicles were quantified. Histograms represent means +/- SEM of 3 independent
906 experiments, 936 WT GFP, 988 WT AKT CA, 1261 WT AKT N, 1357 HTT_{SA} GFP, 1048 HTT_{SA} AKT
907 CA and 1177 HTT_{SA} AKT N vesicles. Significance was determined using one-way ANOVA followed by
908 Tukey's post-hoc analysis for multiple comparisons; * p < 0.05, ** p < 0.01, *** p < 0.001, **** p <
909 0.0001.

910

911 **Figure 5. HTT S421 phosphorylation affects presynaptic APP targeting.**

912 **(A)** Effect of HTT S421 phosphorylation on exocytosis rate of APP was analyzed in COS cells co-
913 transfected with APP-SEP (Super Ecliptic pFluorin) and with pARIS HTT or pARIS HTT_{SA} visualized
914 by TIRF microscopy. Magnification represents a time lapse of events showing 2 events of APP vesicle
915 exocytosis (green arrows). Histograms represent means +/- SEM of exocytosis event number per minute
916 in 39 HTT and 40 HTT_{SA} cells from 4 independent experiments. Significance was determined using an
917 unpaired t-test; * p < 0.05. Scale bar = 20 µm. (see also Video 5). **(B)** Effect of HTT S421
918 phosphorylation on APP targeting at the synapse was assessed by anti-APP western blotting (22C11)
919 analysis of extracts from synaptic chambers of a WT or HTT_{SA} corticocortical network. SNAP25 was
920 used as a control for protein content in the synaptic compartment and nuclear marker Lamin B1 for the
921 somatic compartment. Histograms represent means +/- SEM of APP signal per synaptophysin signal on 5
922 independent experiments. Significance was determined using a Mann-Whitney test; * p < 0.05, ns= not
923 significant. **(C)** Western blotting analysis of pre- and postsynaptic fractions obtained from synaptosome
924 preparations. Fractionation gives the first pellet, P1, the first supernatant, S1, and the second supernatant,

925 S2. Lamin B1, a nuclear marker is enriched in P1 fraction. The pre- (non-PSD) and the post-synaptic
926 (PSD) fractions are respectively enriched in synaptophysin and PSD95. **(D)** APP from WT or HTT_{SA}
927 cortices fractions was quantified by western blotting analyses. APP signal was quantified as the ratio of
928 synaptophysin signal for non-PSD fraction and as the ratio of PSD95 signal for PSD fraction. One line
929 represents one experiment. Significance was determined using Mann-Whitney test; * $p < 0.05$, ns = not
930 significant.

931

932 **Figure 6. HTT dephosphorylation induces changes in brain morphology and synapse number**

933 **(A)** Representative 3D reconstructions of WT brain areas built from high spatial resolution *ex vivo* MRI-
934 T_{1w} data. Each brain structure is represented with a specific color: cortex (purple), hippocampal formation
935 (pink), striatum (green), and other structures (light grey). **(B)** Quantification of the volumes of the
936 different cerebral regions represented in **(A)**. The Graphics show volumes for these regions (in mm³) of 2
937 and 3-month-old WT and HTT_{SA} mice. Black bars represent the mean of 4 WT and 4 HTT_{SA} mice, Mann
938 and Whitney two tails, * $P < 0.05$; ** $P < 0.01$; *** $P < 0.001$. **(C)** Synapse number and size in CA1 region of
939 19-month-old WT or HTT_{SA} mice were quantified by electron microscopy. Axon terminals (AxT) and
940 spines (Sp) are colored with green and purple respectively. Histograms represent means +/- SEM of 3
941 brains with 134 (WT) and 203(HTT_{SA}) fields analyzed and 225 (WT) and 218 (HTT_{SA}) synapses.
942 Significance was determined using an unpaired t-test; ** $p < 0.01$, ns = not significant. Scale bar = 1 μ m.

943 **Figure supplement 1.** Behavioral analyses of the locomotion, force and anxiety in WT and HTT_{SA} mice.

944 **Table supplement 1.** The modified SHIRPA primary screen in WT and HTT_{SA} mice.

945

946 **Figure 7. HTT phosphorylation regulates synaptic contacts by reducing presynaptic APP levels**

947 **(A)** Number of PSD95 / Synaptophysin contacts in the synaptic chamber of WT and HTT_{SA} network.
948 Right microphotographs for each genotype show magnification of representative neurites. Scale bars = 20
949 μ m (low magnification) or 2 μ m (high magnification). Histograms represent means +/- SEM of 3
950 independent experiments and 85 WT and 91 HTT_{SA} neurites. Significance was determined using an
951 unpaired t-test; **** $p < 0.0001$. **(B)** Representative image of APP-mCherry transduced presynaptic
952 neurons. APP is present in axonal terminals positive for synaptophysin (white arrows). Scale bar = 2 μ m.
953 Number of PSD95 / Synaptophysin contacts in the synaptic chamber of WT and HTT_{SA} network
954 transduced at presynaptic site with APP-mCherry or mCherry as a control. Histograms represent means
955 +/- SEM of 3 independent experiments and 75 WT + mCherry; 59 WT + APP-mCherry and 71 HTT_{SA}
956 APP-mCherry neurites. **(C)** Number of PSD95 / Synaptophysin contacts in the synaptic chamber of WT
957 mature network transduced at presynaptic site with a lentivirus encoding an HTT construct containing the
958 first 480 amino acids without (HTT-480-WT) or with the S421A mutation (HTT-480-SA). Histograms

959 represent means +/- SEM of at 3 independent experiments and 132 HTT-480-WT and 130 HTT-480-SA
960 neurites. Significance was determined using Mann and Whitney test; **** $p < 0.0001$. (D) Number of
961 PSD95 / Synaptophysin contacts in the synaptic chamber of WT mature network transduced at
962 presynaptic site with APP-mCherry or mCherry as a control with a lentivirus encoding a HTT-480-WT or
963 HTT-480-SA. Histograms represent means +/- SEM of 3 independent experiments and 132 HTT-480-
964 WT + mCherry, 134 HTT-480-WT + APP mCherry and 136 HTT-480-SA + APP mCherry neurites.
965 Significance was determined using one-way Kruskal-Wallis test followed by Dunn's post-hoc analysis for
966 multiple comparisons; ** $p < 0.01$, *** $p < 0.001$, **** $p < 0.0001$, ns = not significant.

967

968 **Figure 8. HTT S421 dephosphorylation rescues synapse number in APPPS1 mice**

969 (A) APP from APPPS1 and APPPS1/HTT_{SA} cortical fractions were quantified by Western blotting
970 analyses after synaptosomes fractionation. (B) APP signal was quantified as the ratio of synaptophysin
971 signal for non-PSD fraction and as the ratio of PSD95 signal for PSD fraction. Histograms represent
972 means +/- SEM of 9 experiments. Significance was determined using Wilcoxon test; * $p < 0.05$, ns= not
973 significant. (C) Synaptic number and postsynaptic density (PSD) length of CA1 region of hippocampi
974 from 19-month-old APPPS1 and APPPS1/HTT_{SA} mice were quantified by electron microscopy. Axon
975 terminals (AxT) and spines (Sp) are colored with green and purple, respectively. Scale bar = 1 μ m. (D)
976 Histograms represent means +/- SEM of 3 brains; 153 APPPS1 and 152 APPPS1/HTT_{SA} fields and 182
977 APPPS1 and 350 APPPS1/HTT_{SA} synapses were analyzed. Significance was determined using one-way
978 ANOVA followed by Tukey's multiple comparisons test; * $p < 0.05$, **** $p < 0.0001$; ns = not significant.

979 **Figure supplement 1.** Analysis of soluble A β 42 levels, amyloid plaques and amyloid load in APPPS1
980 and APPPS1/HTT_{SA} mice.

981

982 **Figure 9. HTT S421 dephosphorylation enhances learning and memory in APPPS1 mice**

983 (A) Spatial learning of 7 APPPS1 mice (dark blue), 11 APPPS1/HTT_{SA} mice (light blue), and 11 WT
984 mice (black dotted line) was assessed by measuring CIPL (Corrected Integrated Path Length), an
985 unbiased measure of learning in the Morris water maze test over 11 days of training. Data are represented
986 as mean \pm SEM. (B) Cumulative CIPL during the early phase (first 5 days) and the late phase (last 6 days)
987 of training is depicted for WT, APPPS1 and APPPS1/HTT_{SA} mice. All values are means \pm SEM.
988 Significance was determined using one-way ANOVA test followed by Tukey's post-hoc analysis for
989 multiple comparisons; * $p < 0.05$, ** $p < 0.01$, *** $p < 0.001$; ns = not significant. (C) Spatial memory of
990 11 WT, 7 APPPS1 and 11 APPPS1/HTT_{SA} mice was assessed on a probe trial performed 72h after the last
991 training day and during which the percentage of time spent in the target quadrant was quantified. All
992 values are means \pm SEM. Significance above the 25% chance level was determined using a one-sample t-

993 test for each group. * $p < 0.05$, *** $p < 0.001$; ns= not significant. **(D)** Non-spatial memory of 24 WT, 18
994 APPPS1 and 21 APPPS1/HTT_{SA} mice was assessed by the novel object recognition memory test.
995 Memory index is calculated as the percentage of time spent exploring a novel object versus the time spent
996 exploring both familiar and novel objects after a retention interval of 3 hours. All values are means \pm
997 SEM. A score of 50% indicates no preference (i.e., no memory). Performance significantly above the
998 50% chance level was determined using a one-sample t-test for each group. ** $p < 0.01$, *** $p < 0.001$; ns
999 = not significant.

1000 **Figure supplement 1.** Behavioral analyses of the locomotion and anxiety in WT, APPPS1 and
1001 APPPS1/HTT_{SA} mice.
1002

1003 **Supplemental Methods**

1004 **Vesicular fractionation**

1005 Three 6/7-month-old mice were used per genotype. The protocol was adapted from (Zala et al.,
1006 2013). Briefly, frozen brains were homogenized in 700 μ L of homogenization buffer (320mM sucrose) by
1007 triturating with a Dounce homogenizer. Then, samples were centrifuged twice at 47,000 rcf for 10
1008 minutes and the two supernatants were combined (S1). From S1, another ultracentrifugation was
1009 performed at 120,000 rcf for 40 minutes to obtain S2 and P2. The S2 fraction was put in another tube and
1010 280 μ L of 700mM sucrose buffer was added under the S2 fraction. After a 2 hours centrifugation at 260
1011 000 rcf, S3 and P3 were obtained. P3 fraction was resuspended in 50 μ L of Re-suspension buffer (10 mM
1012 HEPES pH 7.3 and 320 mM sucrose). Antibodies used for western blot analysis are KHC (clone SUK4,
1013 Covance; MMS-188P,) and p150 (BD Transduction Laboratories, 610474).

1014

1015 **Primary Screen (modified SHIRPA)**

1016 The testing was carried out using a modified version of the standard protocol (Rogers et al., 1997). HTT_{SA}
1017 and WT littermate control mice were examined at 12 months of age. The primary screen began by
1018 observing undisturbed behavior in a viewing jar (clear Perspex cylinder, 15 cm x 11 cm) for 30 s (section
1019 1). Thereafter, the mouse was transferred in the arena (55 cm x 33 cm x 18 cm) for testing of transfer
1020 arousal and observation of normal behavior (section 2). The observer also looked for any manifestation of
1021 bizarre or stereotyped behavior, convulsions and indications of spatial disorientation. This was followed
1022 by a sequence of manipulations using tail suspension and the grid across the width of the arena (section 3).
1023 To complete the assessment, the animal was restrained in a supine position to record autonomic behaviors
1024 (section 4).

1025

1026 **Open field activity (OF)**

1027 The open field test was used to assess locomotor activity (and anxiety-related behaviors). Mice were
1028 tested in a homogeneously illuminated (50 lux) circular open field arena made of white plastic (diameter:
1029 54 cm) with 30 cm-high walls. Monitoring was done by an automated video tracking system (AnyMaze,
1030 Stoelting, Wood Dale, IL, USA). The main behavioral parameters analyzed during a single 10 minute
1031 session in the OF were the total traveled distance and also the center-to-periphery exploration ratio.

1032

1033 **Grip force test**

1034 Mice were scruffed by the lower back and lowered towards a mesh grip piece attached to a force gauge
1035 (Bioseb) until the animal grabbed it with both front paws. The animal was then lowered toward the

1036 platform and gently pulled straight back with consistent force until it released its grip. The forelimb grip
1037 force was recorded on the strain gauge.

1038

1039 **Elevated plus maze (EPM)**

1040 The EPM was made of beige PVC and the center of the field illuminated at 70 lux. The apparatus was
1041 elevated 50 cm above floor level and consisted of four arms (35 cm × 5 cm). Two of the arms contained
1042 15 cm-high walls (enclosed arms) and the other two had no walls (open arms). Each mouse was placed in
1043 the middle section facing an open arm and left to explore the maze for a single 5 min session with the
1044 experimenter out of view. Animals were video-recorded and their behavior automatically analyzed with
1045 the ANY-maze software. Percent time spent in open arms which is supposed to be inversely correlated to
1046 anxiety levels was measured for each mouse.

1047

1048 **Neuropathology**

1049 Following completion of behavioral testing, at 19 months of age, mice were anaesthetized with
1050 pentobarbital (120 mg/kg) and then transcardially perfused with phosphate-buffer saline solution. The
1051 brain was extracted and carefully weighed on a precision balance. One hemisphere was snap frozen in
1052 liquid nitrogen and then stored at -80°C for subsequent biochemical analysis. The other half brain was
1053 fixed by immersion in freshly-made formaldehyde solution (3-4 days), then cryoprotected in a 2 % -
1054 DMSO – 20 % glycerol solution and finally cut on a freezing microtome (serial sections of 40 µm of the
1055 entire brain).

1056 Amyloid deposits were labeled by standard Congo red staining (30 min in an 80% ethanol solution
1057 saturated with Congo red and sodium chloride). Microscopic scans of whole sections (pixel size 0.25
1058 µm²) were acquired with a NanoZoomer 2.0-RS slide scanner (Hamamatsu Photonics, Hamamatsu,
1059 Japan). Amyloid loads were quantified using computer-based segmentation methods using the spot
1060 detector plugin of the ICY software (<http://icy.bioimageanalysis.org>) that automatically calculates the
1061 proportion of stained tissue ($p = \text{stained area} / \text{total area}$), providing unbiased stereological measurements.

1062 **Immunolabelling**

1063 For immunostaining, free-floating sections were washed in PBS 0.1M to remove cryoprotectant. The
1064 sections were treated with hydrogen peroxide for 10 min to quench endogenous peroxidase activity,
1065 permeabilized with 0.25% Triton X-100 in PBS 0.1M (PBSTx) for 20 min, pre-incubated in a 5% PBS-
1066 Tx normal goat serum (NGS) blocking solution and then incubated overnight at room temperature (RT)
1067 with the following primary antibodies : a biotinylated mouse anti-A β (**4G8**) (1:3000, Covance Antibody
1068 Products), a rabbit polyclonal antibody recognizing amyloid fibrils and fibrillary A β oligomers (**OC**)

1069 (1:3000, StressMarq Biosciences) and a rabbit polyclonal anti-prefibrillar A β oligomers (**A11**) (1:1000,
1070 generous gift of Dr. Kayed Rakez). The sections were incubated with a secondary biotinylated goat anti-
1071 rabbit antibody at RT for 90 min (this step was omitted for 4G8 antibody that was already biotinylated).
1072 Tissues were then incubated in the Vector Elite avidin-biotin peroxidase kit (1:800) for 90 min at RT.
1073 Finally, after washes in PBS-Tx and Tris 0.1M solutions, immunoreactivity was revealed using
1074 diaminobenzidine (DAB) as chromogen to visualize the reaction product. The sections were then mounted
1075 on Superfrost slides, dehydrated in a series of alcohols (30%, 50%, 70%, 2x 90% and 2x 100%), cleared
1076 in xylene, and coverslipped with EUKITT mounting medium.

1077

1078 **Analysis**

1079 Microscopic scans of immunostained brain sections were acquired with a **NanoZoomer 2.0-RS slide**
1080 **scanner** (Hamamatsu Photonics) at 40X magnification (pixel size 0.25 μm^2). Selected regions of interest
1081 (ROIs) were delineated by using the Paxinos and Franklin Mouse Brain Atlas: sensori-motor (SM),
1082 Frontal (FR) and the hippocampus (HPC). ROIs were assessed across 2 to 6 consecutive serial sections
1083 (depending on structure) and were manually outlined on digitized sections. Computer-based segmentation
1084 methods were applied for 4G8 and OC immunostaining using the Best threshold plugins of the **ICY**
1085 software (<https://icy.bioimageanalysis.org>) that automatically calculate the proportion of stained tissue
1086 ($p = \text{stained area} / \text{total area}$) in each ROIs. For A11 immunostained sections, A β loads were calculated
1087 using the **Ilastik** interactive learning and segmentation toolkit software (<https://ilastick.org/index.html>).
1088 The frontal cortex, the sensori-motor cortex and the hippocampus brain regions were manually outlined
1089 on digitized sections. To evaluate the 4G8-detected A β loads, reference background staining of the corpus
1090 callosum was used to binarize the digitized image to 8-bits black and white image. The mean number of
1091 thresholded pixels per ROI was automatically calculated using an ICY image analysis software script. A
1092 minimum of 3 sections per brain ROIs per animal were analyzed and counting's were reported to the
1093 overall ROI surface to provide the 4G8 amyloid loads.

1094

1095 **A β 42 dosages**

1096 Hemi-forebrains (~200 mg) were harvested in 500 μl of solution containing 50 mM Tris-HCl (pH 7.6),
1097 0.01% NP-40, 150 mM NaCl, 2 mM EDTA, 0.1% SDS, 1 mM phenylmethylsulfonyl fluoride (PMSF),
1098 and protease inhibitor cocktail (Sigma). Soluble, extracellular-enriched proteins were collected from
1099 mechanically homogenized lysates following centrifugation for 10 min at 3,000 g. Cytoplasmic proteins
1100 were extracted from cell pellets mechanically dissociated with a micropipettor in 500 μl buffer containing
1101 50 mM Tris-HCl (pH 7.6), 150 mM NaCl, 0.1% Triton X-100 following centrifugation 90 min at 11,000
1102 g. Supernatant was collected for dosages. Supernatants from cortical neurons plated in microchambers

1103 were collected on ice in polypropylene tubes (Corning, Corning, NY, USA) containing a protease
1104 inhibitor cocktail (Roche) and were then stored at -80°C Concentration of A β peptides were measured by
1105 Electro-Chemiluminescence Immuno-Assay (ECLIA) performed according to the manufacturer's
1106 instructions Meso Scale Discovery (MSD). Briefly, samples were analyzed using MSD SECTOR™
1107 Imager 2400 (Meso Scale Discovery, Gaithersburg, MD, USA), with the Rodent A β triplex kit (from
1108 MSD) on carbon 96-well plates. 100 μ l of blocking buffer solution were added to avoid non-specific
1109 binding. The plates were then sealed, wrapped in tin foil, and incubated at room temperature on a plate
1110 shaker (300 rpm) for 1 h. Wells were then washed three times with washing buffer, and 25 μ l of the
1111 standards and samples were then added to the wells, followed by an A β -detecting antibody at 1 μ g/ml
1112 (MSD) labelled with a Ruthenium (II) trisbipyridine N-hydroxysuccinimide ester; this detection antibody
1113 was 4G8. Plates were then aspirated and washed 3 times. MSD read buffer (containing TPA) was added
1114 to wells before reading on the Sector Imager. A small electric current passed through a microelectrode
1115 present in each well producing a redox reaction of the Ru²⁺ cation, emitting 620 nm red light. The
1116 concentration of A β was calculated for each sample, using dose–response curves, the blank being cell-less
1117 culture medium. All the conditions were tested in duplicate. A β levels were normalized with total amount
1118 of proteins quantified by Bradford dosage.

1119

1120 **Supplemental References**

1121

1122 Rogers, D.C., Fisher, E.M., Brown, S.D., Peters, J., Hunter, A.J., and Martin, J.E. (1997). Behavioral and
1123 functional analysis of mouse phenotype: SHIRPA, a proposed protocol for comprehensive phenotype
1124 assessment. *Mamm Genome* 8, 711-713.

1125 Zala, D., Hinckelmann, M.V., Yu, H., Lyra da Cunha, M.M., Liot, G., Cordelieres, F.P., Marco, S., and
1126 Saudou, F. (2013). Vesicular glycolysis provides on-board energy for fast axonal transport. *Cell* 152, 479-
1127 491.

1128

1129

1130

1131 **Supplementary legends**

1132

1133 **Figure 1-figure supplement 1.** Time course of kinetics of anterograde and retrograde APP-mCherry
1134 axonal velocity after plating neurons into microchambers. DIV = day in vitro. Data are represented by
1135 means +/- SEM of three independent experiments minimum and 314 vesicles per condition.

1136

1137 **Figure 3-figure supplement 1.** Vesicular distribution of kinesin and dynactin in WT and HTT_{SA} mouse
1138 brains. Total, vesicular and cytosolic fractionations were analyzed by western blot using KHC, p150
1139 (fractionation control) and Tubulin (loading control) antibodies. (A) KHC signal was quantified in total
1140 fraction as the ratio of KHC signal on tubulin signal. (B) Vesicular KHC signal was normalized on
1141 cytosolic signal. Graphs represent 3 brains per genotype analyzed with 2 independent experiments.
1142 Significance was determined using Mann-Whitney test. p=0,09

1143

1144 **Figure 6-figure supplement 1.** Behavioral analyses of the locomotion, force and anxiety in WT and
1145 HTT_{SA} mice. Behavioral analyses of the locomotion, force and anxiety in WT and HTT_{SA} mice (A)
1146 Locomotor activity and the anxiety-related behavior of 19-month-old HTT_{SA} mice (n= 12) and WT
1147 littermate controls (n=11) were quantified as the total distance travelled in the open field arena (left) and
1148 by the ratio of time spent in the periphery over the center of the arena in the open field (right). All values
1149 are means ± SEM. Significance between groups was determined with an unpaired t-test; ns= not
1150 significant. (B) Grip strength of HTT_{SA} mice and WT littermate controls was evaluated by the grip force
1151 test. All values are means ± SEM. Significance between groups was determined with an unpaired t-test;
1152 ns= not significant. (C) Anxiety-like behavior of HTT_{SA} mice (n= 12) and WT littermate controls (n= 9)
1153 was assessed by the elevated plus maze test. All values are means ± SEM. Significance between groups
1154 was determined with an unpaired t-test; ns= not significant.

1155

1156 **Figure 8-figure supplement 1.** Analysis of soluble Aβ42 levels, amyloid plaques and amyloid load in
1157 APPPS1 and APPPS1/ HTT_{SA} mice. (A) Soluble Aβ42 levels were measured in APPPS1 and APPPS1/
1158 HTT_{SA} mouse brains 19-month-old. The data are represented as means ± SEM. Significance was
1159 determined using Mann-Whitney test; ns= not significant. (B) APPPS1 and APPPS1/HTT_{SA} coronal brain
1160 sections from 19-month-old mice were immunostained with the 4G8 antibody to visualize amyloid
1161 plaques. Scale bar = 2 mm. (C) Amyloid loads in in APPPS1 mice (n= 9) and APPPS1/HTT_{SA} mice (n=
1162 12) were measured in coronal brain sections from the sensori-motor cortex (S-M), frontal cortex (Fr), and
1163 hippocampus (HPC) using Congo red histochemistry, 4G8 antibody, anti-Aβ fibrillary Aβ oligomers

1164 (OC), and anti-prefibrillar A β oligomers (A11). Data were analyzed using a Two-way ANOVA and are
1165 represented as mean \pm SEM; ns= not significant.

1166

1167 **Figure 9-figure supplement 1.** Behavioral analyses of the locomotion and anxiety-related behavior in
1168 WT, APPPS1 and APPPS1/HTT_{SA} mice. **(A)** Locomotor activity of 19-month-old WT (n=23), APPPS1
1169 (n=18) and APPPS1/HTT_{SA} (n=23) mice was assessed by the total distance travelled in the Open field
1170 arena. The data are represented as mean \pm SEM. Significance was determined using a one-way ANOVA;
1171 ns= not significant. **(B)** Anxiety-related behavior of WT (n=23), APPPS1 (n=18) and APPPS1/HTT_{SA}
1172 (n=23) mice was evaluated by the time spent in the periphery versus center of the open field arena. All
1173 values are means \pm SEM. Significance was determined using a one-way ANOVA; ns= not significant.

1174

1175 **Table supplement 1.** The modified SHIRPA primary screen in WT and HTT_{SA} mice. Results are
1176 presented in percentages unless otherwise indicated. No significant differences between genotypes were
1177 observed.

1178

1179 **Video 1.** Axonal Transport of APP-mCherry in Presynaptic Cortical Neurons at DIV13. Vesicles were
1180 recorded for 60 sec at 5 Hz. Axons are oriented from soma (top of the channel) to neurite terminals
1181 (bottom) with anterograde vesicles going down. Scale bar, 20 μ m.

1182

1183 **Video 2.** Transport of APP-mCherry (right panel) in MAP2-GFP Positive Postsynaptic Cortical Dendrites
1184 (left panel) at DIV13. Vesicles were recorded for 60 sec at 5 Hz. Dendrites are oriented from soma (top of
1185 the channel) to neurite terminals (bottom) with outward vesicles going down. Scale bar, 20 μ m.

1186

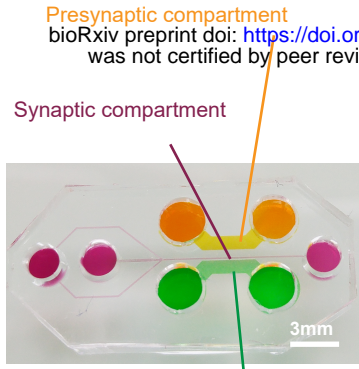
1187 **Video 3.** APP-mCherry transport in Wild-Type (left panel) or HTT_{SA} (right panel) axons at DIV13.
1188 Vesicles were recorded for 60 sec at 5 Hz. Axons are oriented from soma (top of the channel) to neurite
1189 terminals (bottom) with anterograde vesicles going down. Scale bar, 20 μ m.

1190

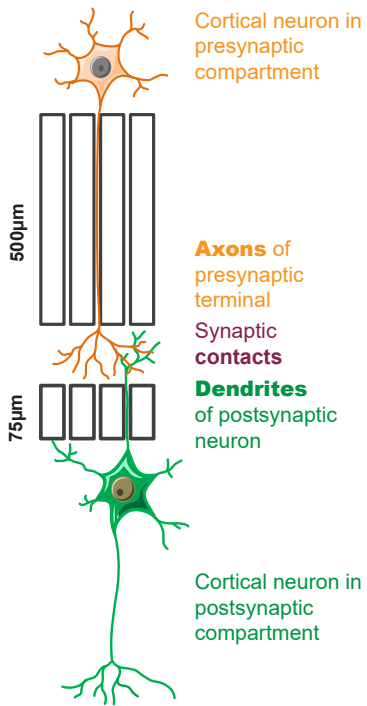
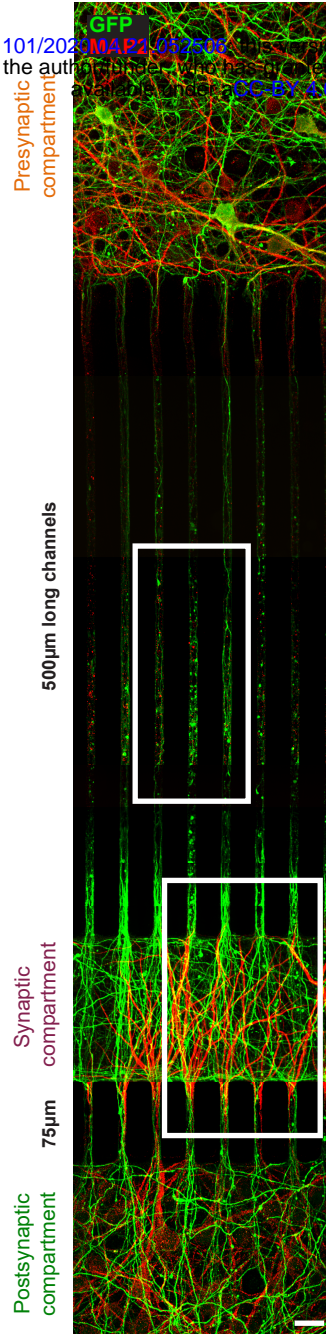
1191 **Video 4.** Effect of Akt on the Axonal Transport of APP-mCherry in Presynaptic Cortical Neurons from
1192 Wild-Type or HTT_{SA} mice at DIV13. Vesicles were recorded for 60 sec at 5 Hz. Axons are oriented from
1193 soma (top of the channel) to neurite terminals (bottom) with anterograde vesicles going down. Scale bar,
1194 20 μ m.

1195

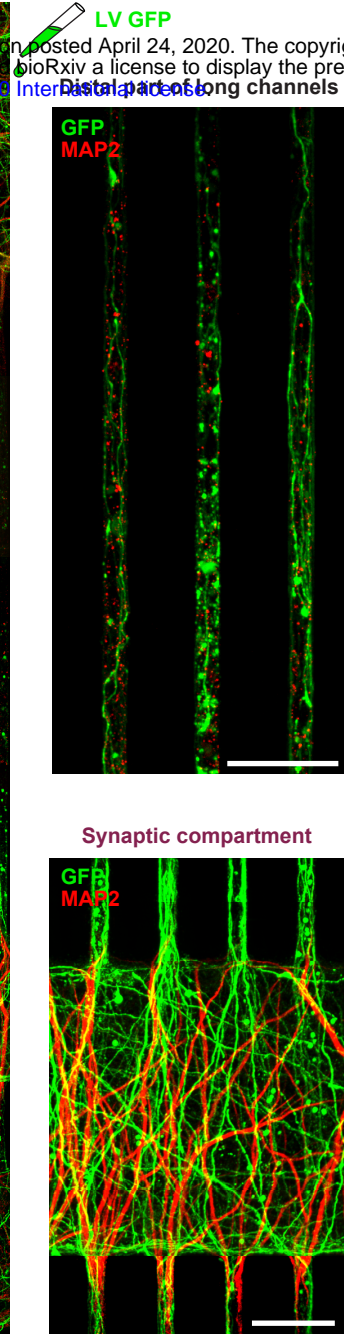
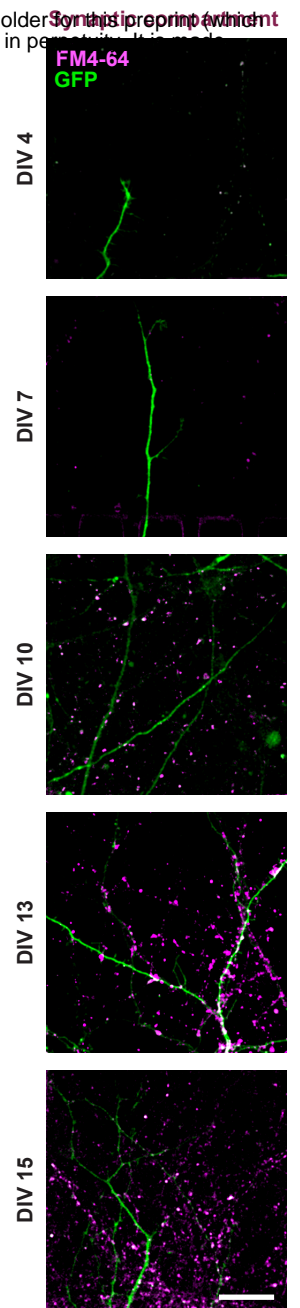
1196 **Video 5.** APP-SEP co-transfected in COS cells with pARIS WT (left panel) or pARIS HTT_{SA} (right
1197 panel) visualized by TIRF microscopy. Vesicle exocytosis of APP was recorded at 5 Hz. Scale bar, 20
1198 μm .

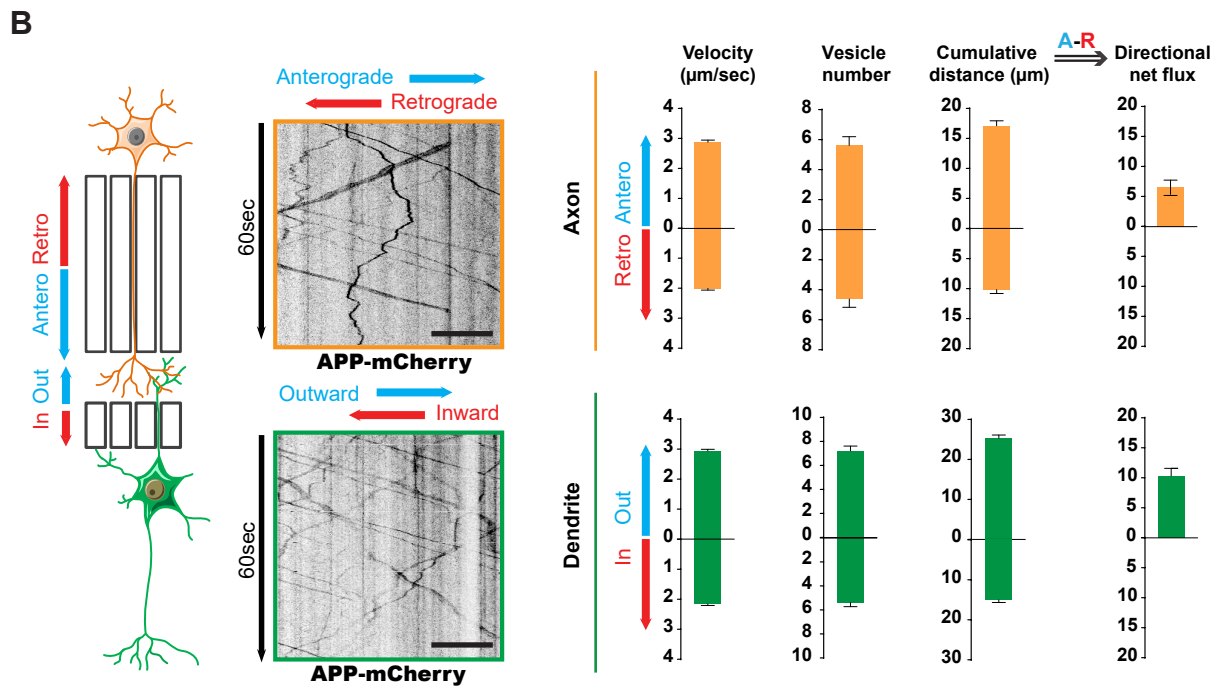
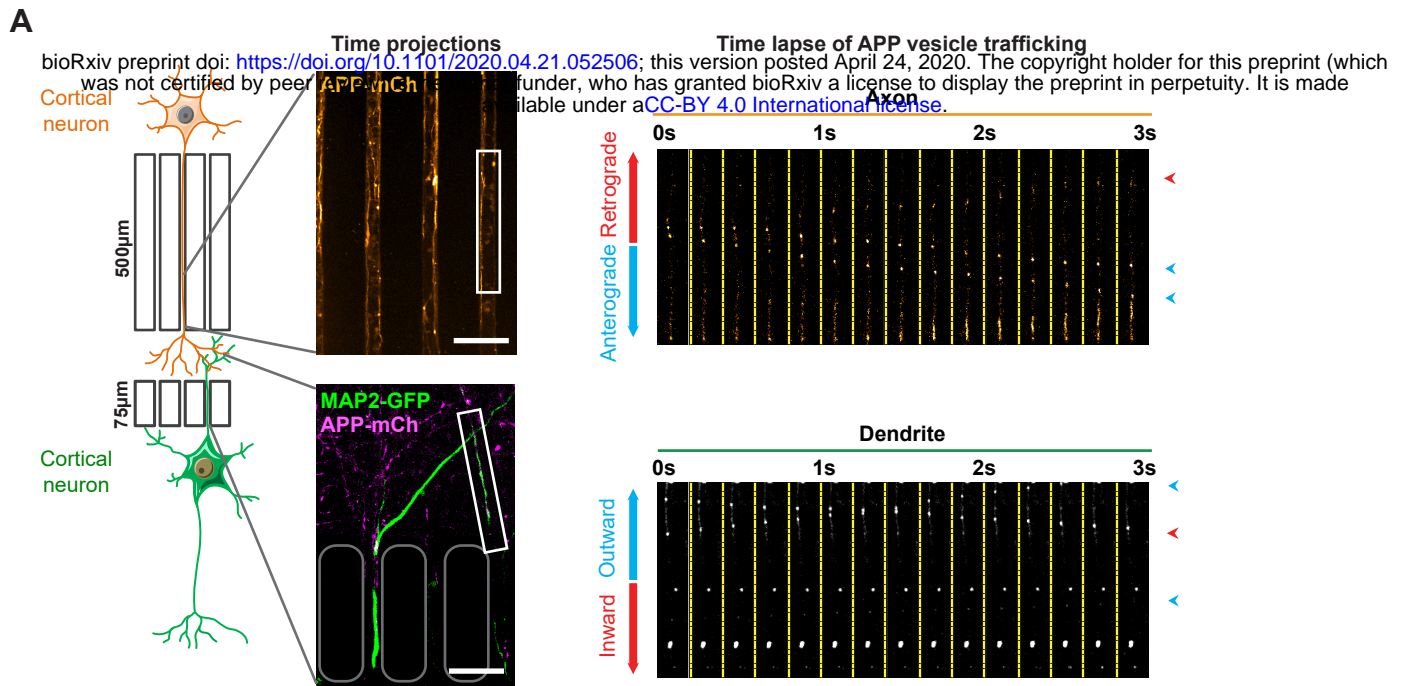
A

Postsynaptic compartment

**B**

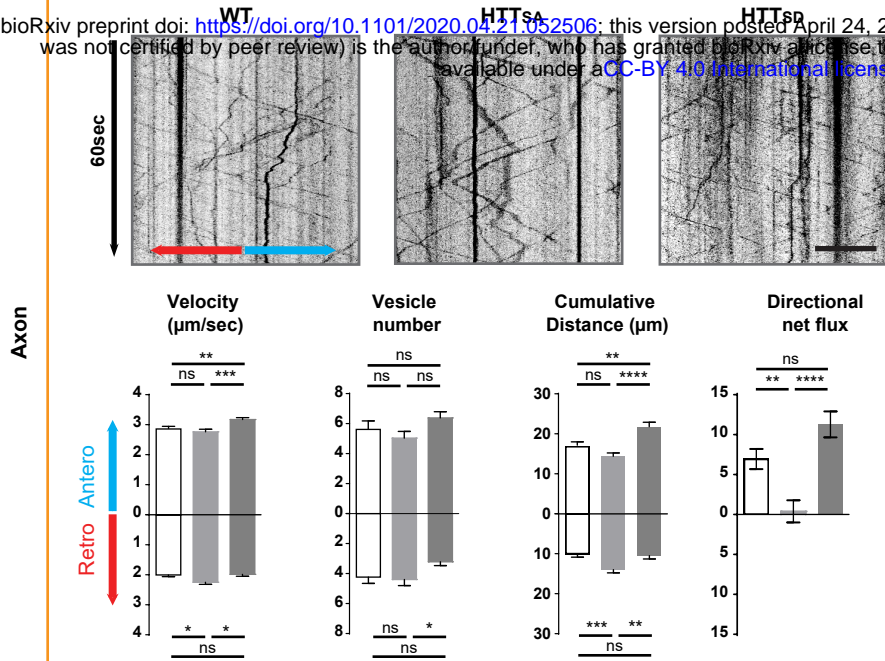
bioRxiv preprint doi: <https://doi.org/10.1101/2020.04.25.052508>; this version posted April 24, 2020. The copyright holder for this preprint (which was not certified by peer review) is the author/funder, who has granted bioRxiv a license to display the preprint in perpetuity. It is made available under aCC-BY 4.0 International license.

**C**

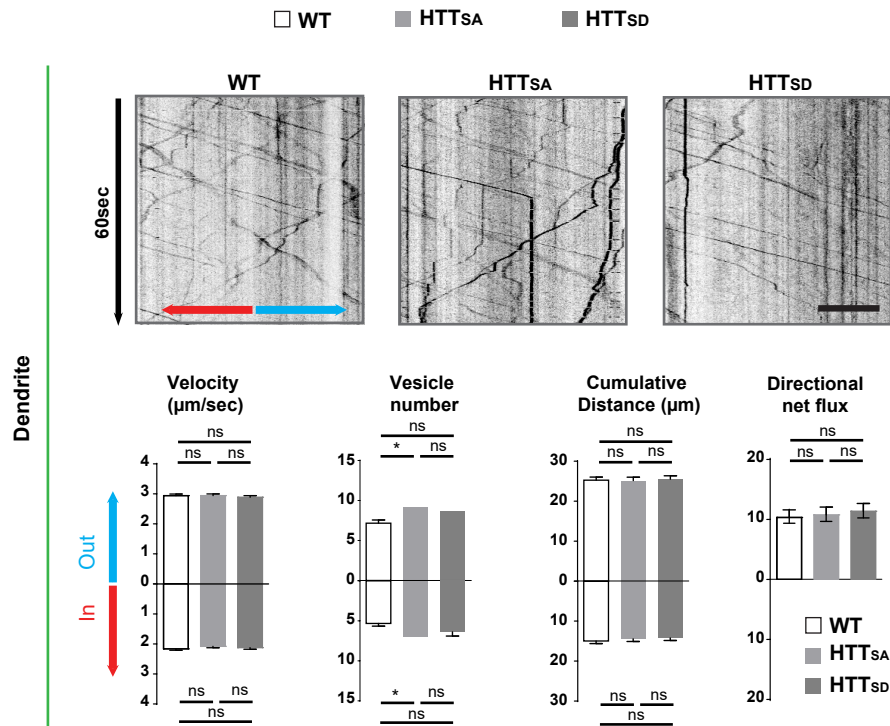


A

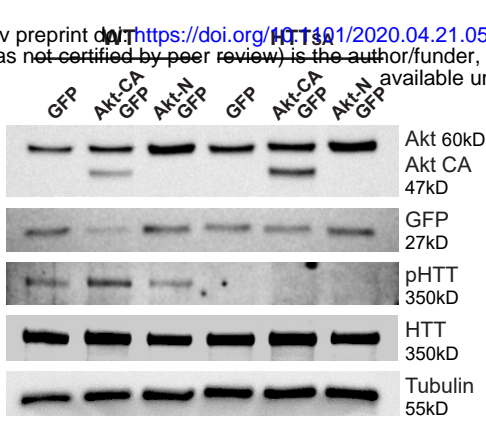
bioRxiv preprint doi: <https://doi.org/10.1101/2020.04.21.052506>; this version posted April 24, 2020. The copyright holder for this preprint (which was not certified by peer review) is the author/funder, who has granted bioRxiv a license to display the preprint in perpetuity. It is made available under aCC-BY 4.0 International license.



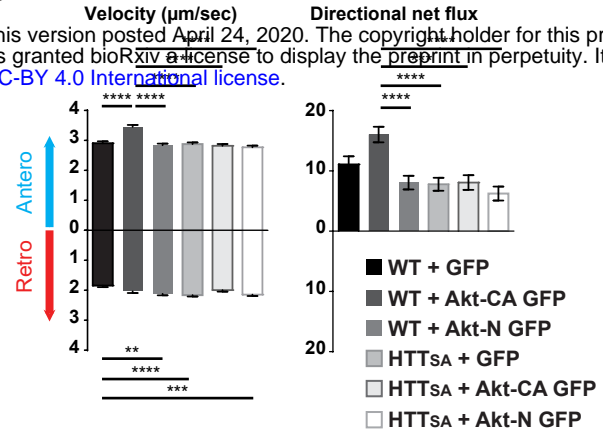
B



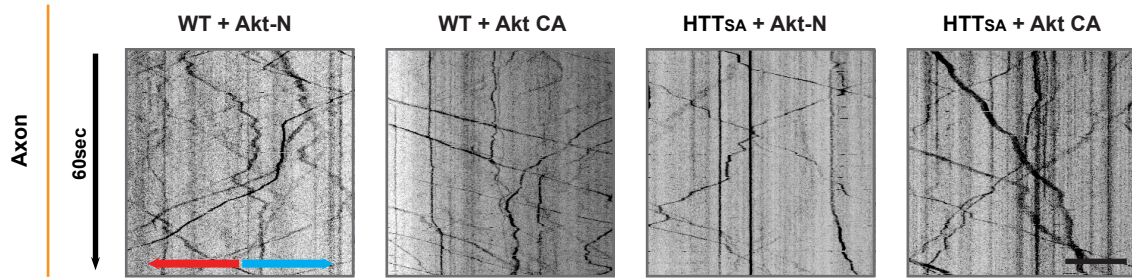
A

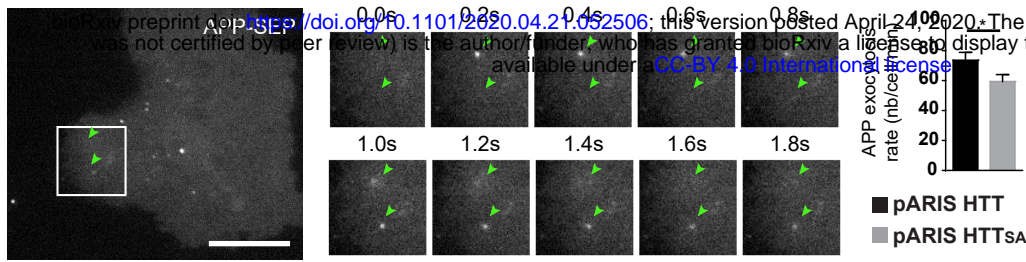
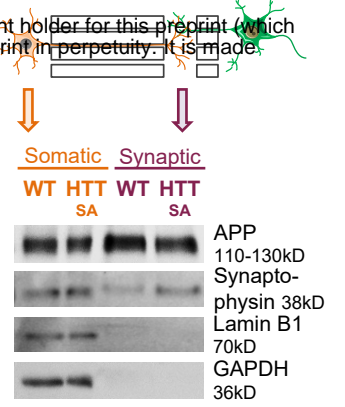
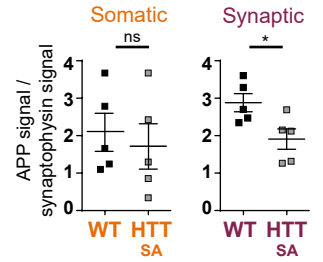
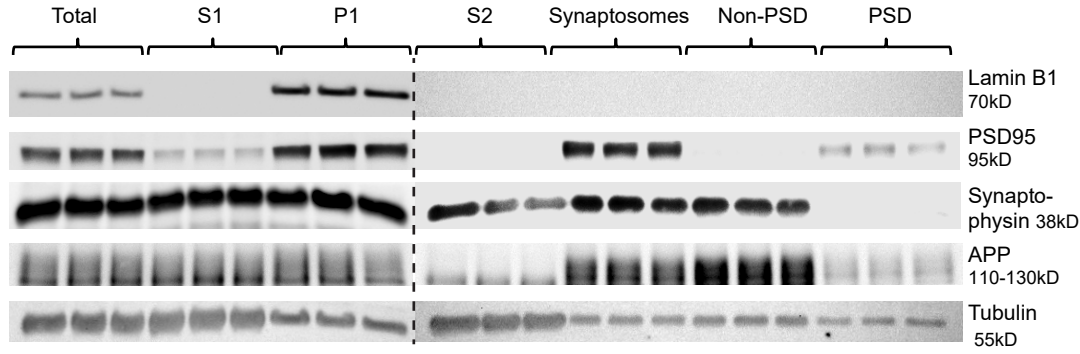
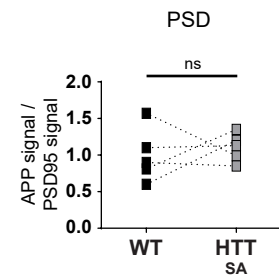
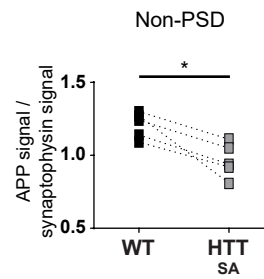
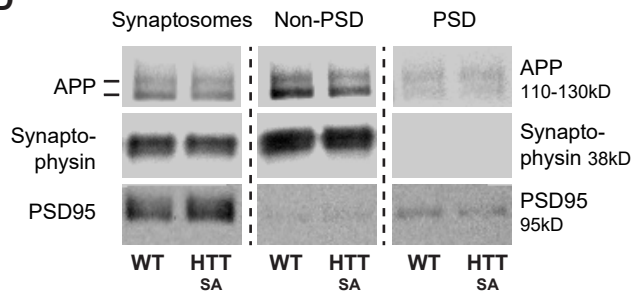


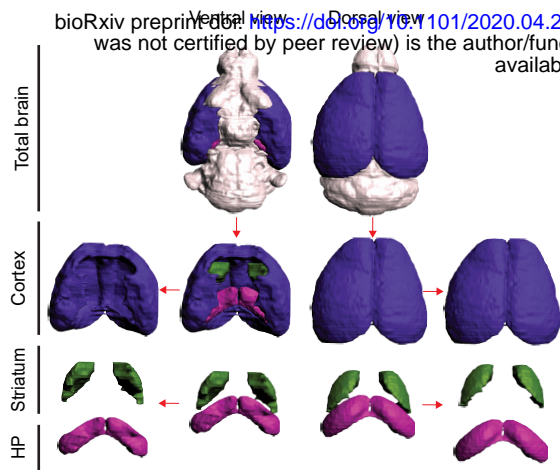
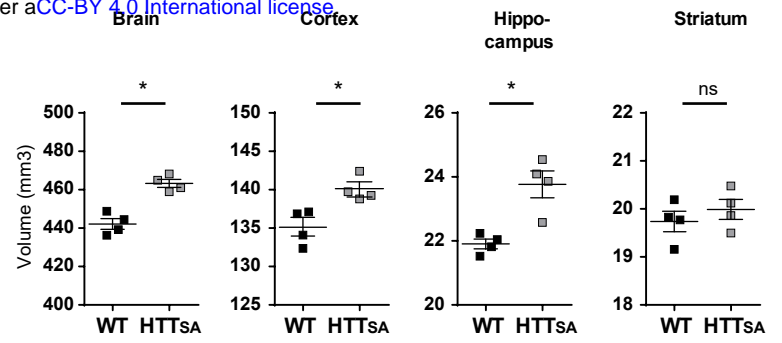
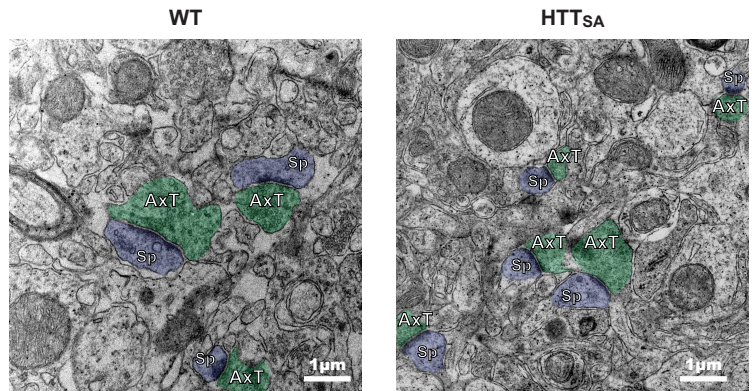
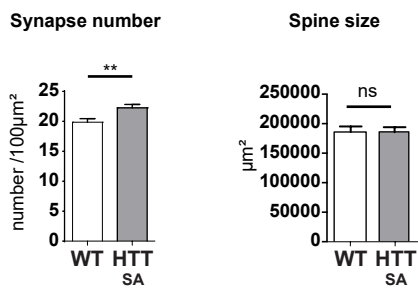
C

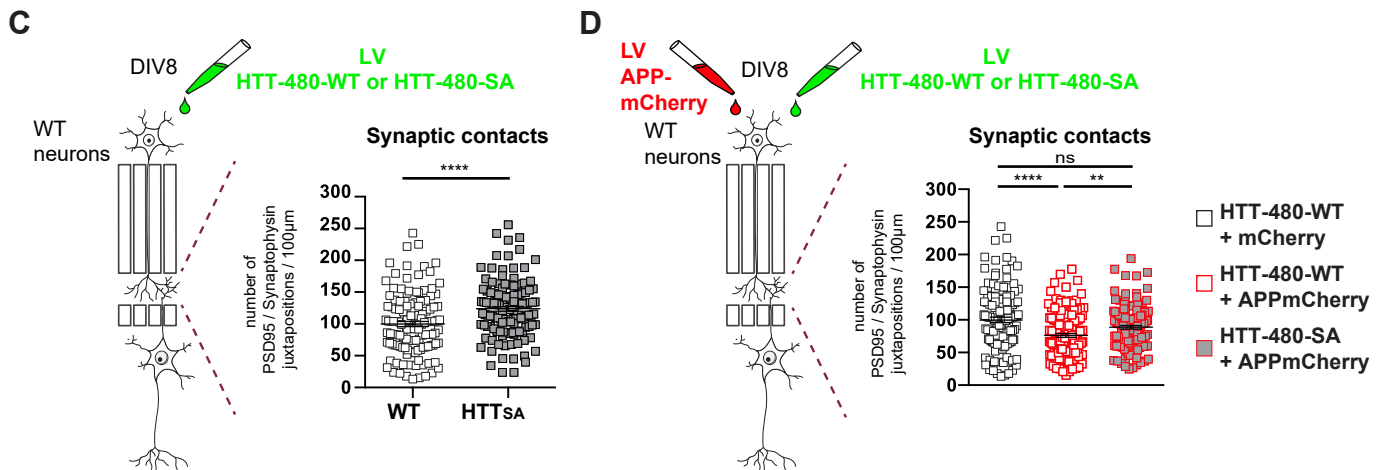
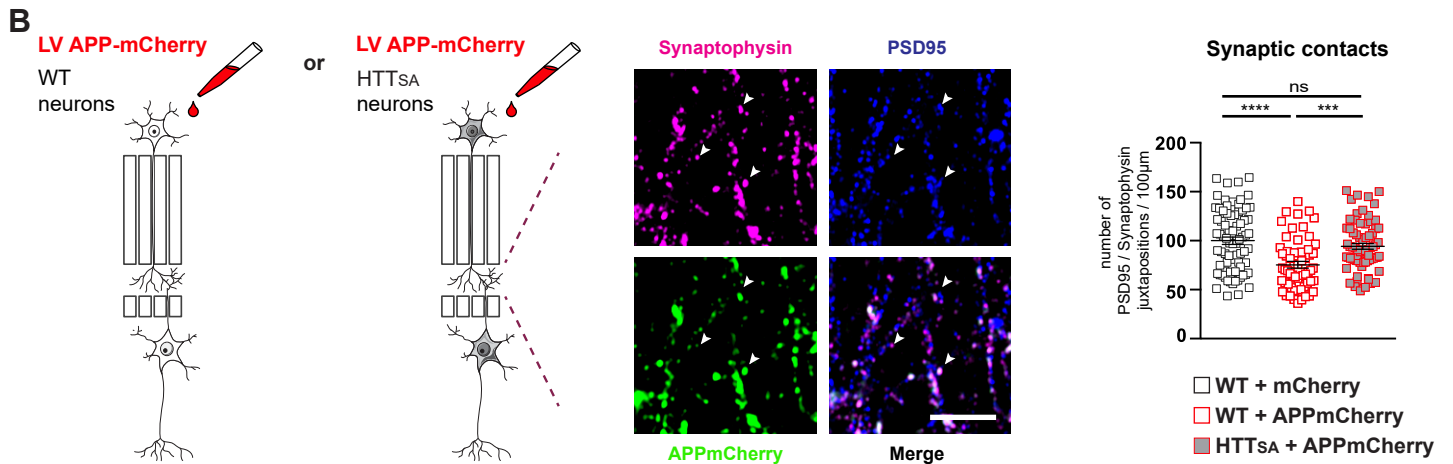
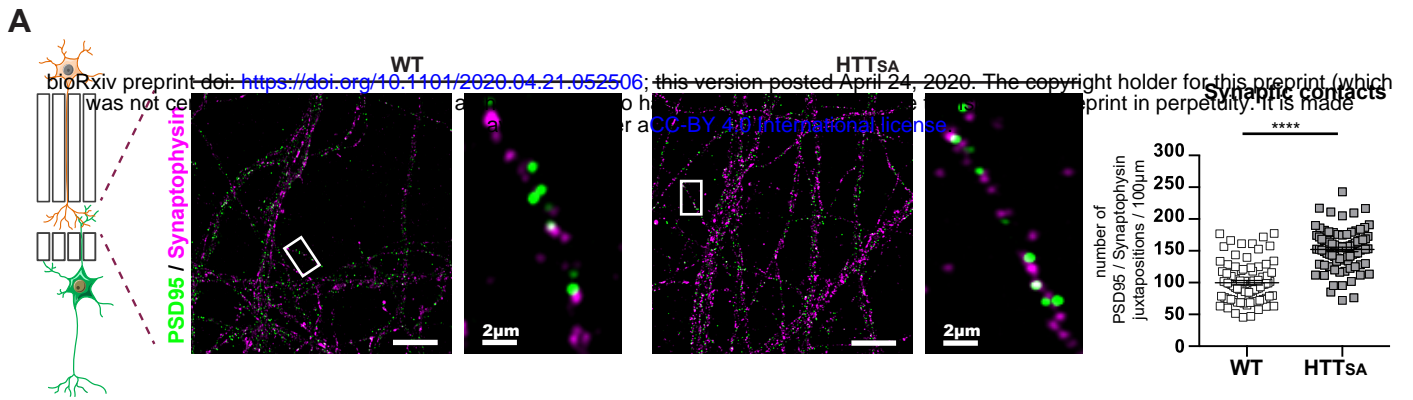


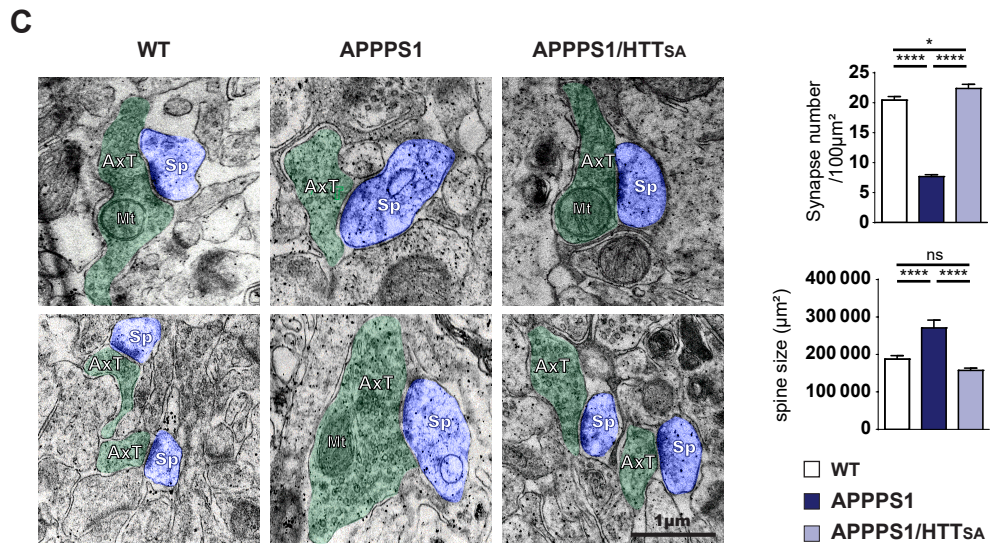
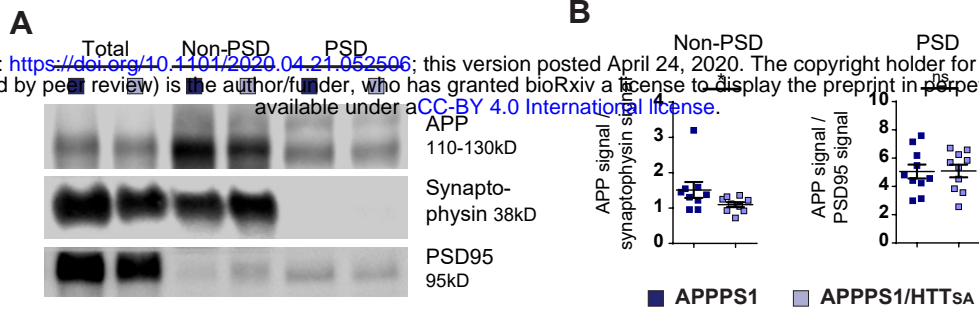
B



A**B****C****D**

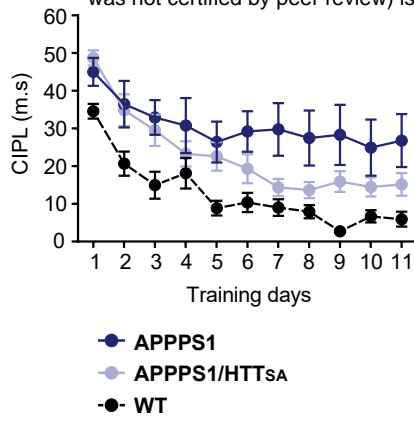
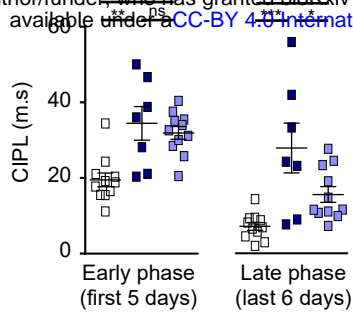
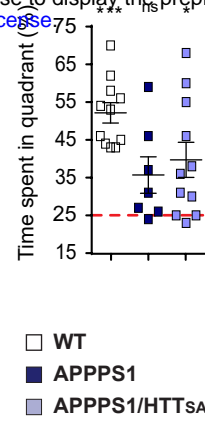
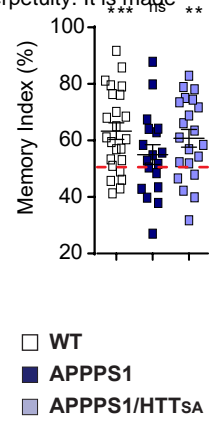
A**B****C**



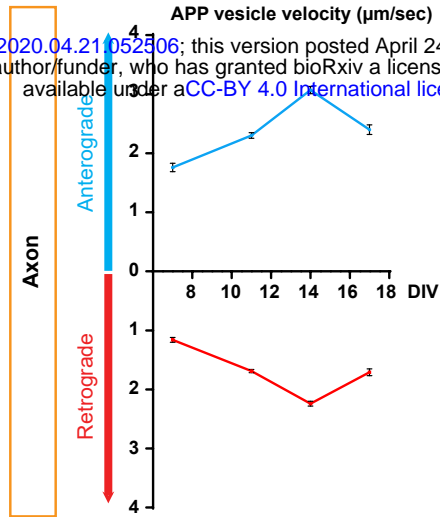


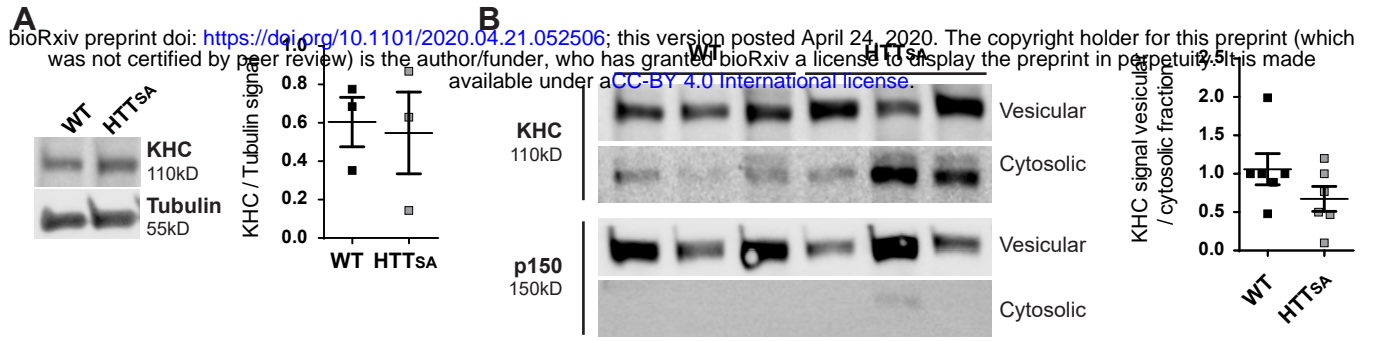
A**Spatial Learning**

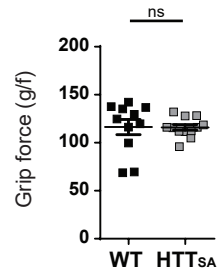
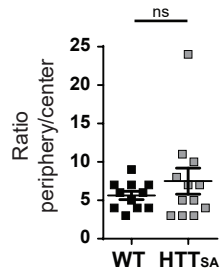
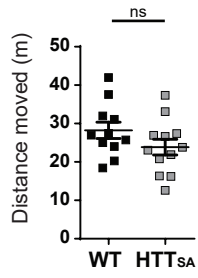
bioRxiv preprint doi: <https://doi.org/10.1101/2020.04.21.052506>; this version posted April 24, 2020. The copyright holder for this preprint (which was not certified by peer review) is the author/funder, who has granted bioRxiv a license to display the preprint in perpetuity. It is made available under aCC-BY 4.0 International license.

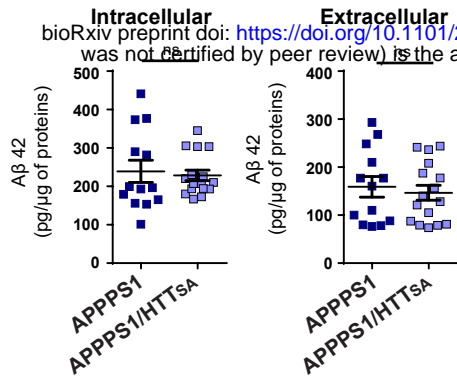
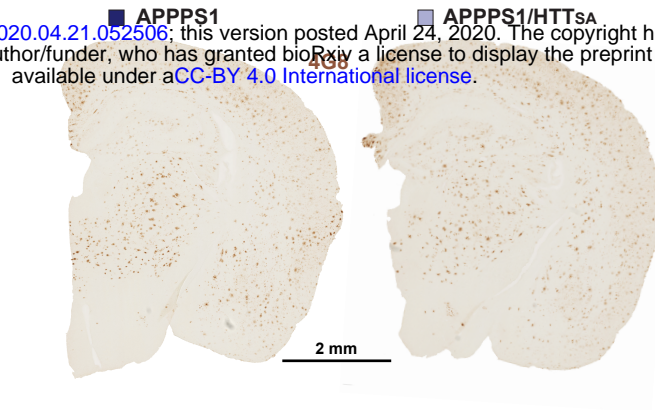
**B****Spatial Learning****C****Spatial Memory****D****Non-Spatial Memory**

bioRxiv preprint doi: <https://doi.org/10.1101/2020.04.21.052506>; this version posted April 24, 2020. The copyright holder for this preprint (which was not certified by peer review) is the author/funder, who has granted bioRxiv a license to display the preprint in perpetuity. It is made available under aCC-BY 4.0 International license.







A**B****C**